Effect of Mn Interfacial Doping in Polycrystalline Thin Films

By

Robert Carpenter

Submitted for the Degree of Master of Science

The University of York

Department of Physics

November 2011

Abstract

In this study the York Model has been used to find the origin of the increase in the exchange field (H_{ex}) when 1-2 atomic layers of Mn are added to the interface of CoFe/IrMn polycrystalline sputtered thin films. The structures studied were Si(100)/Ta(5nm)/Ru(5nm)/IrMn(10nm)/Mn(*x*nm)/CoFe(2nm)/Ta(5nm) where x = 0, 0.3, 0.6, 0.9, 1.2 and 1.5. In the case of 0.3 and 0.6nm of Mn an increase in H_{ex} was found, whilst the addition of further Mn caused a decrease. The blocking temperature distribution $f(T_B)$ and the grain volume distribution $f(V)$ were measured for each sample in order to calculate the AF grain anisotropy (K_{AF}). No significant variation was observed in $f(T_B)$ with the addition of Mn suggesting that the change in H_{ex} is solely due to variations at the interface. This was confirmed as a change in H_{ex} of ~125Oe was observed with an increase in the initial setting field (H_{set}) from 5kOe to 20kOe was found for samples with the additional layer of Mn.

Contents

Table of Figures

Acknowledgments

I should start off by thanking both Kevin and Western Digital. Without Kevin I would have had no teacher and the sheer amount of physics I feel I have learned in the past year thanks to him still surprises me. Without the financial support of Western Digital I would not have been able to fund my time here and so for that I am extremely grateful.

As for the content of this piece of work I should thank a number of people for their various inputs. Nick, who started in the topic essentially at the same time as me, has been invaluable during the whole process as sometimes the best teacher is a fellow student. Next in line is Barbara who helped me achieve some form of competence in the operation of the HiTUS in the earlier days whilst also helping me to point in the right directions with my work. As far as my education in microscopy and the associated sample prep goes the combined efforts and abilities of James, Jessada and Luke have been exceedingly helpful. Alex also deserves mention. Even though he is in a different field his skills as a scientist, as well as just being a great guy, have made the overall process that much easier and entertaining.

On a personal level I would like to thank my friends who stuck around for another year of physics to complete their MPhys courses as without them it would have been a significantly duller experience. Specifically I would like to thank Mark and Chris for both letting me bounce ideas…but also keeping my knowledge base that bit broader. Finally I would like to thank Juliet. There isn't much I can say to express it but she knows.

Declaration

I declare that the work presented in this thesis is based purely on my own research, unless otherwise stated, and has not been submitted for a degree in either this or any other university.

Signed

Robert Carpenter

Chapter 1. Introduction

The effect of Exchange Bias was first discovered in 1956 by Meiklejohn and Bean [1]. Whilst investigating the properties of core-shell oxide nanoparticles they observed an increase in the coercivity and a shift in the hysteresis loop for the case of Co/CoO after field cooling in a saturating field. The original result obtained is shown in figure 1. Meiklejohn and Bean explained this loop shift as a uniaxial exchange anisotropy caused by the exchange interaction between the Ferromagnetic (F) Co and its Antiferromagnetic (AF) CoO oxide shell.

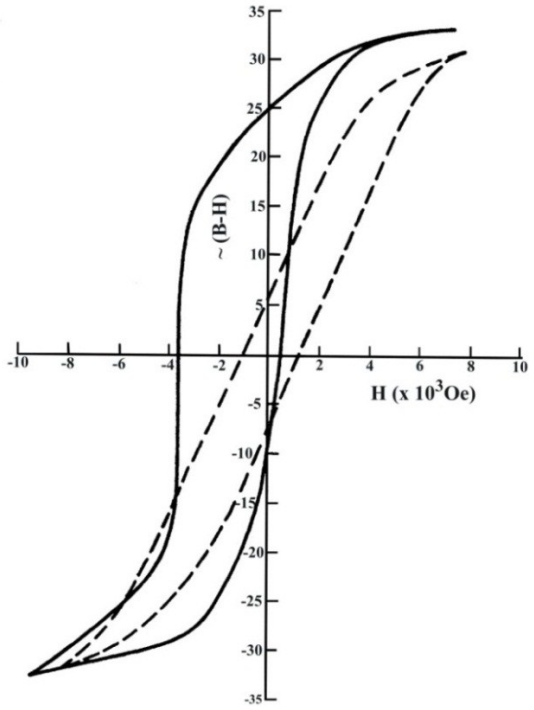

Figure 1: Hysteresis loops of Co compacts fine coated in CoO measured at 77K. The solid curve occurs when the sample is cooled in an applied saturating field whilst the dashed curve is when it is cooled with no applied field [1].

Over the years there have many attempts at modelling the effect with what can only be described as varying levels of failure. Part of this problem arose due to the comparison of epitaxial thin films, polycrystalline thin films and core-shell particles each of which possesses very different interfacial geometries. In the case of epitaxial films the interface is flat with atomic steps whilst core-shell particles will have curved and very rough interfaces. Polycrystalline thin films sit in the middle with a grain size dependant interfacial roughness as shown in figure 2. As exchange bias is highly dependent on the F/AF interface attempting to apply, for

example, an epitaxial thin film model to a polycrystalline sample will give incorrect predictions.

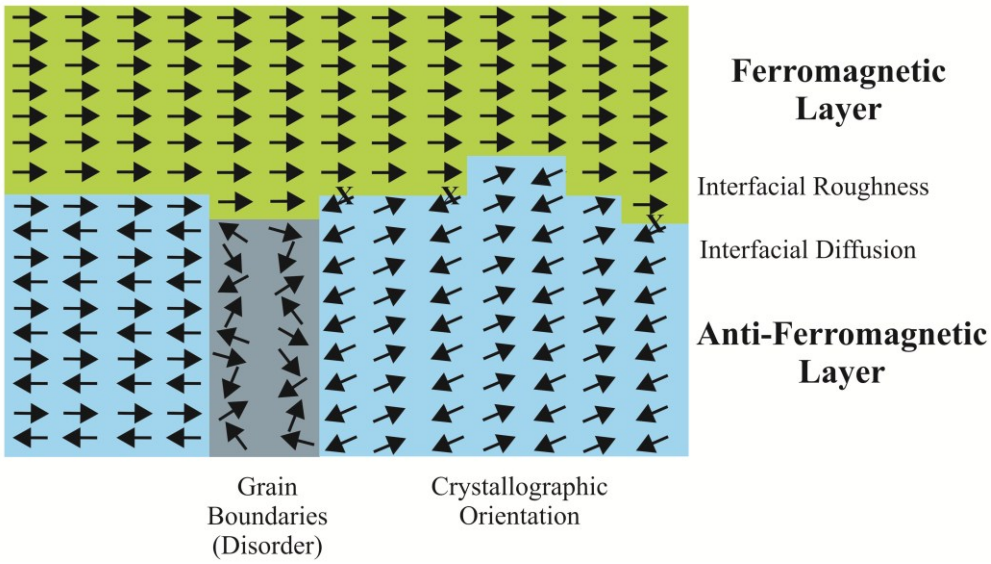

Figure 2: Diagram showing some of the complexities present at the interface of an exchange biased system. The X marks signify the frustrated exchange bonds i.e. the interfacial spins that are coupled anti-ferromagnetically [2].

As the AF layer is subject to thermal instabilities, specifically at room temperatures, results obtained from measuring the exchange bias will depend critically upon the measurement conditions. Throughout the literature little care has been taken to ensure thermal stability of the samples creating a certain level of uncertainty about the accuracy of results. This is a result of the non-reproducibility of normal DC measurements.

A recent review by O'Grady et al. has addressed these issues with the development of the York Model and the associated York Protocols [3]. The model was initially developed solely for sputtered polycrystalline thin films but has since been expanded to cover multiple domain systems [4]. The York protocols were designed to measure and control the thermal stability of the AF layer allowing for reproducibility of results. The work in this thesis utilizes the explanations derived from this model and was carried out using the York Protocols.

1.1. Technological Significance

When exchange bias was originally discovered it was merely of academic interest. However with the discovery of Giant Magnetoresistance (GMR) by Grünberg and Fert [5] in 1988 it became vital in the technical application of GMR. GMR occurs when the magnetisation of neighbouring F layers are orientated in opposition. The mechanism through which this occurs is spin dependent scattering. Metallic ferromagnets possess the spin split band structure that leads to the spin dependent scattering required for GMR. An availability of unoccupied states in the part-filled d bands of the ferromagnetic transition metals allows the easy scattering of electrons reducing their mean free path. Mott [6] states that in transition metals the spin-up and spin-down electrons can be considered as independent current channels. In the spin-split d bands responsible for ferromagnetism there is a difference in density of states at the Fermi surface for spin-up and down electrons which leads to a difference in scattering probability. The minority spin electrons are the most likely to be scattered in this case. This results in the spin filtering of an electric current when passed through a F material.

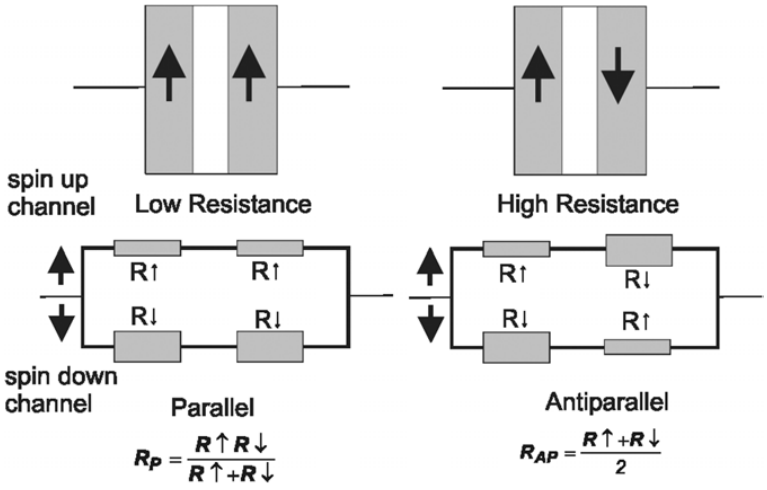

Figure 3: Schematic demonstrating the parallel circuit behaviour of the two spin channels when passing through two F layers [5].

The case of a simple magnetic tri-layer can be modelled using a resistor network as shown in figure 3. The resistance (R) of the different layers is represented by equation (1) where the independent spin-up and spin-down currents are taken to be two circuits in parallel.

$$\frac{\Delta R}{R} = \frac{R_{AP}-R_P}{R_P} = \frac{(R\downarrow - R\uparrow)^2}{4R\downarrow R\uparrow} \quad (1)$$

In the left hand scenario where the two F layers are aligned parallel both spin channels experience very different scattering. One of the spin currents will be the minority electron channel whilst the other will be the majority electron channel. The minority spin channel will undergo significant scattering in both layers whilst the majority spin channel will be much less scattered. The conductivity is then predominantly carried by the majority spin channel and so overall resistance is lower. In the right hand case where the F layers are antiparallel both spin currents will be the majority and minority spin channels as they go through the two layers. Therefore both currents undergo the same scattering and the combined resistance of the structure is higher [5].

GMR is observed when the orientation of the two F layers in a magnetic structure can be switched from parallel to antiparallel switching the circuit resistance from high to low. This situation can be achieved by using the difference in the coercive field between two materials or by taking advantage of the thickness dependence of interlayer exchange coupling. By pinning one of the layers through exchange bias a large difference in switching field can be obtained for the two layers. The utilisation of exchange bias in GMR systems has led to the development of the spin-valve [5].

A spin valve consists of an F layer pinned by the exchange field from an attached AF layer. This pinned F layer is then separated from a free F layer by a non-magnetic spacer. The free layer tends to be a soft F that can be easily switched in a small field. The spin valve has a number of technological applications examples of which will be explained in the following chapters.

1.1.1. The Magnetoresistive Read Head

Just less than ten years after the discovery of GMR hard disk drives (HDD) with GMR read heads were produced. Resolution of data reading has increased drastically since its inception and has allowed for smaller bit sizes to be used. Simultaneously the saturation magnetisation requirements' have decreased therefore reducing the demagnetising field which has allowed for an increase in the data density.

A schematic of a read/write head is demonstrated in figure 4. The head is suspended above the media using the aerodynamics of the head generated by the 3.6-15k rpm speeds of the disk. The bit pattern is written into the magnetic medium through the reversal of the grains that compose a bit. The write head does this by generating a magnetic field that penetrates the recording layer. A soft magnetic under layer is utilised in order to achieve higher write fields and hence storage densities e.g. in modern drives utilising this technology densities of up to 1Tb per square inch have been achieved [7]. In order to prevent detection of stray fields the GMR sensor is placed between two magnetic shields. Exchange bias is used to pin a F layer whilst an unpinned layer in the sensor is free to rotate under the magnetic field of the bits in the medium providing a GMR system. A current is passed through the sensor in order to measure the variations in the magnetoresistance. As such by measuring the magnetic bit pattern a current pattern is produced.

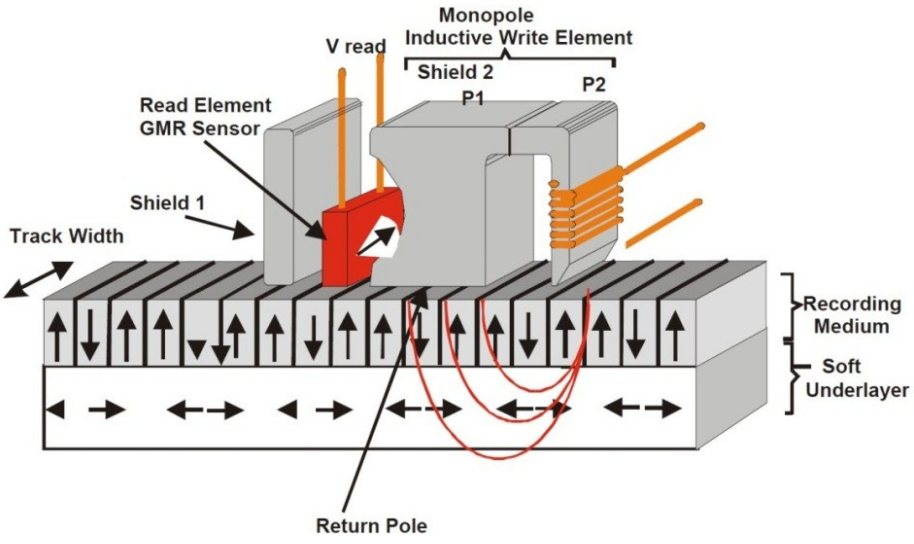

Figure 4: Schematic of a Hard Disk Drive (HDD) read/write head [8].

In order to decrease the size of the read head the strength of the pinned layer had to be improved. Substantial research was carried out in order to improve AF materials. In the 1980's and 90's the AFs available such as FeMn and NiO had weak exchange energies and poor thermal stability. The current AF of choice is IrMn due to its high anisotropy of 900K [9] and resistance to corrosion. Due to the underpinning nature of exchange bias for GMR the massive growth of the magnetic storage industry led to massive steps in the fundamental understanding of the area.

1.1.2. Magnetic Random Access Memory

Throughout the 1950's to 1970's magnetic core memory was the predominant computer memory. With the advent of semiconductor FET(DRAM) memories in the mid 1970's magnetic based memory lost its prominence. Apart from specialised components for military and aerospace systems little interest was paid towards the development of magnetic memories. With the discovery of GMR and the development of the spin-valve the concept of magnetic random access memory (MRAM) was proposed. A review of the history of chip development can be found in [10] and different approaches to the topic in [11]

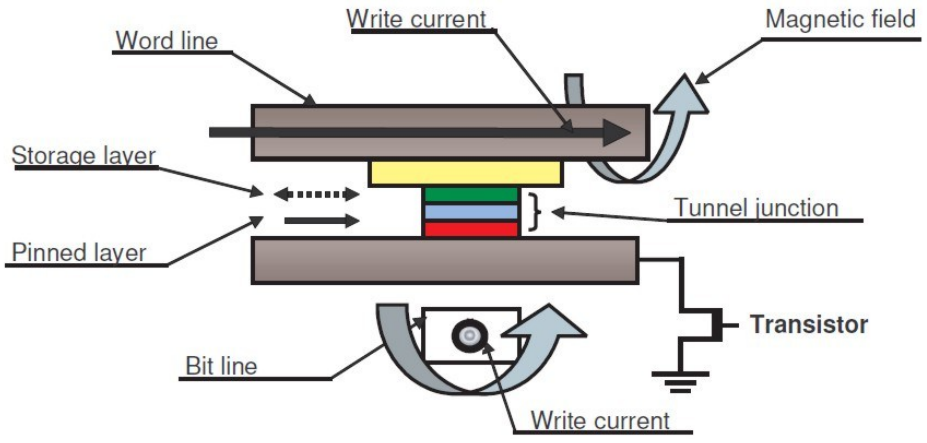

Figure 5: Simple schematic of how a single 'bit' is stored in an MRAM device.

Figure 5 shows a simple schematic of an early MRAM device. Much like in the aforementioned GMR sensor information is stored in the orientation of the storage layer in comparison to the pinned layer. The magnetic orientation of the storage layer is varied by running currents down the word and bit lines. The state of the bit is then measured by passing a current through the stack and measuring the

resistance. The advantages of such a system over standard DRAM is that the data stored is non-volatile and so is not only energy efficient but the systems of data storage and memory could be combined.

A flaw in this design, however, is that the method of writing data can affect neighbouring cells decreasing the potential data density. The word and bit lines can be eliminated by taking advantage of current induced magnetisation reversal [12]. When a current is passed through a F layer the electrons become polarised parallel to the magnetisation whilst anti-parallel spins are scattered. These electrons can maintain their polarisation whilst passing through a nonmagnetic spacer and upon entering another F layer can transfer their angular momentum acting as a torque. Under certain conditions, such as high current densities, this can reverse the magnetisation of the material. Thus it is possible to use the read current to simultaneously write [11].

Chapter 2. Magnetism of Thin Films

The magnetic materials used in this study were sputtered polycrystalline thin films with a bi-layer structure of $Co_{35}Fe_{65}/Ir_{20}Mn_{80}$. In order to properly interpret the results obtained a good understanding of the underlying mechanisms is required. In this first chapter the fundamental underlying mechanisms of ferromagnetism and antiferromagnetism will be covered followed by a chapter that covers the current state of theories on exchange bias.

2.1. Exchange Interactions

In 1906 Pierre Weiss advanced his hypothesis on 'Molecular Field Theory' in order to explain the large disparity between the magnetisation of paramagnets and ferromagnets when under an applied field. Weiss proposed the situation in which a material is paramagnetic and solely under the influence of a molecular field H_m proportional to the magnetisation [13] as defined by

$$H_m = \gamma M \tag{2}$$

At a constant temperature the plot of magnetisation vs. applied field will intersect with equation (2) at two points: zero and some value of M. The zero point is unstable as a field no matter how small will be sufficient to magnetise the sample. At that new magnetisation H_m will be larger than M as seen in equation (2), which then applies a greater field on the sample increasing M which further increases H_m. This will continue up until the second intersect which using the same logic is shown to be stable. This material has therefore undergone spontaneous magnetisation up to the saturation magnetisation (M_s) of the sample at the specific temperature. This is the behaviour observed in F. This leads to the view that a F is merely a paramagnet with a very large molecular field [13].

Above the Curie temperature (T_c) the molecular field is overcome and a F will behave paramagnetically. Therefore there is a temperature dependence to the value of M_s. Assuming that the molecular field acts on a material with a relative magnetisation determined by the quantum-mechanical Brillouin function $B(J,a')$, where J is the total angular momentum quantum number and $a' = \mu_H H/kT$, the relative spontaneous magnetisation σ_s/σ_0 can be described as [13]

$$\frac{\sigma_s}{\sigma_0} = \tanh\frac{(\sigma_s/\sigma_0)}{(T/T_c)} \quad (3)$$

The Weiss theory of the molecular field very accurately predicts the behaviour of Ferromagnetism however does not provide a hypothesis on the origin of the field. This origin was not understood until 1928 when Heisenburg [14] proposed that the causation of the molecular field was due to quantum-mechanical exchange forces.

2.1.1. Direct Exchange

The exchange interaction is a result of the Pauli Exclusion Principle when applied to two atoms as a whole. The principle states that two identical fermions, in this case electrons, cannot possess the same energy and spin. In the situation of the hydrogen molecule the two atoms are in such close proximity that their two electrons can have the same velocity and occupy the same space, however to accommodate this they must have opposite spin. If the spins are parallel the Coulomb Electrostatic Energy is modified by the spin orientation which implies a fundamental electrostatic origin [13].

This exchange energy was shown by Heisenburg to play an important role in ferromagnetism. If two atoms *i* and *j* possess spin angular momentum $S_i h/2\pi$ and $S_j h/2\pi$ then the exchange energy between them is

$$E_{ex} = -2J_{ex}S_i \cdot S_j = -2J_{ex}S_i S_j \cos\phi \quad (4)$$

where J_{ex} is the exchange integral and ϕ is the angle between the spins. If J_{ex} is positive then E_{ex} is at a maximum when the spins are antiparallel and a minimum when parallel. As ferromagnetism is due to the parallel alignment of spins on adjacent atoms a positive value of J_{ex} is required.

It is important to note that the step from the two atom system in equation (4) to crystalline Fe is a massive one and the calculation of E_{ex} is currently impossible. Many semi-quantative results have been obtained however. The Bethe-Slater curve shown in figure 6 shows the variation of the exchange integral with the ratio r_a/r_{3d} where r_a is the atomic radius and r_{3d} the radius of the 3d shell of electrons. The distance between two atomic cores in a solid is $2r_a$ and so if two atoms of the same type are brought closer with no change in r_{3d} the ratio will decrease. As the 3d electrons approach one another the J_{ex} becomes increasingly positive,

favouring parallel spins, and then decreases to zero. A further decrease in the interatomic spacing brings the 3d electrons so close that J_{ex} becomes negative and so the spins become anti-parallel. This gives rise to the effect of antiferromagnetism as observed in Mn and Cr below their Néel temperature. This will be explained in depth in section 2.4.

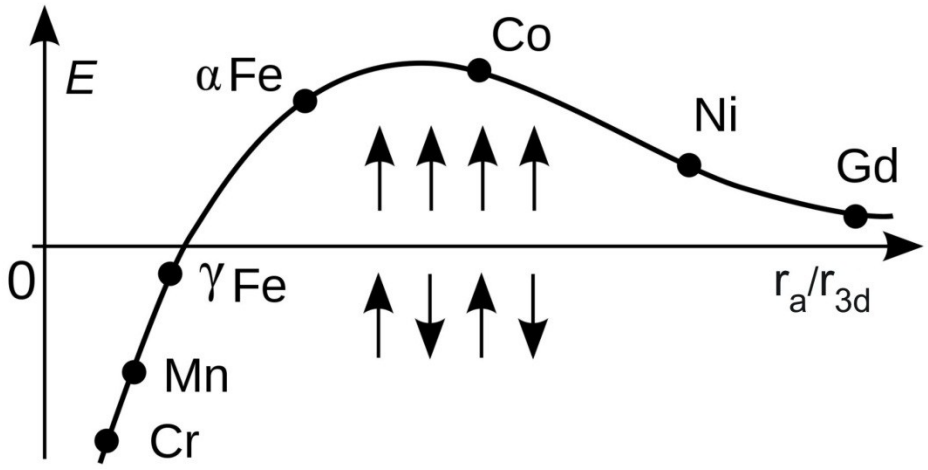

Figure 6: Schematic of the Bethe-Slater curve [13].

2.1.2. Indirect Exchange

The coupling of localised magnetic moments in a metal relies on the ability of conduction electrons to interact magnetically with the local moments and propagate between different magnetic sites. The mechanism of how the conduction electrons polarise and propagate was shown by Ruderman and Kittel in 1954 [15]. The theory was extended into s-f and s-d interactions by Kasuya [16] and Yosida [17] and subsequently became known as RKKY theory.

In a metal the localised magnetic moments sit on specific lattice sites and are surrounded by a cloud of conduction electrons. The region in which the local moment sits will favour conduction electrons of parallel moment whilst those with antiparallel moments will experience the inverse. As such a parallel electron will distort its wave function by mixing in other electron states of the same spin so it is larger within the vicinity of the localised moment. The added wave functions are such that they are in phase so that they interfere constructively at the position of the local moment. As they must possess different wave vectors the wave functions

will begin to interfere destructively as the distance from the localised moment increases. This results in the distribution of parallel electrons having an oscillatory nature. The exact inverse occurs for the antiparallel electrons and so the charge density remains the same. As the periodicity of the spin density oscillations is controlled by the conduction electrons at the Fermi level it is dominated by the Fermi momentum [13].

If a second atom with a local magnetic moment is placed at some arbitrary distance from the initial atom whether it interacts ferromagnetically or antiferromagnetically is dependent on it being in the positive or negative part of the original polarisation wave. RKKY theory states that the strength of the magnetic coupling between atoms at a relatively large distance R_A varies according to [13]

$$(1/R_A^3)\cos(2k_F R_A) \tag{5}$$

where k_f is the Fermi momentum. This shows that the magnetic interaction has a much larger range than that of direct exchange. It is however very sensitive to the interatomic distance and the periodicity of the spin density.

2.2. Magnetic Domains

The exchange interaction on its own is insufficient to explain ferromagnetism due to its inability to explain the common existence of F materials in their unmagnetised state. In answer to this Weiss proposed that F materials are actually composed of many small domains that are individually magnetised to saturation. The direction of these magnetisations varies from domain to domain so the overall net magnetisation of the F material will be zero. The mechanism of magnetisation then becomes one of forcing the multiple domains into a single state aligned with that of the applied field.

When two domains are magnetised in different directions there must be some form of transition between them, this is called the domain wall. The deciding factors of both the domain wall thickness and energy are the exchange energy and anisotropy energy. According to equation (6) the exchange energy for two atoms with the same total spin, *S*, is

$$E_{ex} = -2JS^2\cos\phi \tag{6}$$

In order to decrease E_{ex} the change in spin between domains will occur gradually over a number of intermediate grains so that ϕ is minimised. By expanding $cos\phi$ it can be found that [13]

$$E_{ex} = JS^2\phi^2 - 2JS^2 \tag{7}$$

Where $JS^2\phi^2$ is the extra energy within the wall per spin pair.

The magneto-crystalline anisotropy, as described in section 2.3.1, also defines the domain wall thickness. As there will be a number of spins pointing in a non-easy direction the crystal anisotropy energy within the wall will be greater than that of the adjoining domains. As such the domain walls width will be constrained in order to decrease the number of spins pointing in the non-easy direction. The anisotropy energy of the wall is therefore the constant of the anisotropy K_F times the volume of the wall. Therefore per unit area [13]

$$\gamma_{an} = K_F N a \tag{8}$$

where a is the area of the domain wall and N is the number of atoms within the wall. The combination of these energies gives a domain wall that has a thickness dependent on the crystal structure and atom type. Taking into account the exchange energy of the domain wall the minimum thickness is given by

$$\delta = \sqrt{\frac{JS^2\pi^2}{K_F a}} \tag{9}$$

It has been found experimentally that domain wall thicknesses vary from 50nm to many hundreds of nm. However in materials having very high magnetocrystalline anisotropy (K_F > 2x10^6 ergs/cc) domain wall widths can be reduced to a few nm. This will be the case in large grain AF materials such as IrMn. However in this study the AF grains are single domain. This is because the diameter of the AF grains and thickness of the AF layer are well under that of any reported domain wall widths. Therefore it is exceedingly unlikely for there to be any domain wall formation within the grains.

2.3. Anisotropy

As the structural properties of a material can be inhomogeneous the magnetic properties are similarly not uniform across the sample. The term anisotropy is used to describe this feature as the magnetic properties will vary depending on the direction at which you measure the sample. There are many types of anisotropy: magneto-crystalline, shape, stress and exchange anisotropy as well as anisotropies induced by: magnetic annealing, plastic deformation and irradiation. As the two more dominant anisotropies are magneto-crystalline and shape they will be covered in more detail. The exchange anisotropy is the subject of this study and the following chapter will describe it in more detail.

2.3.1. Magneto-Crystalline Anisotropy

The most fundamental of the anisotropies is that of magneto-crystalline anisotropy due to its dependence on the crystal structure of the material. The physical origin of the magneto-crystalline anisotropy lies in the interaction of the magnetic moment spin to the electron orbital shape and orientation which is known as spin-orbit coupling. The electron orbital shape is of course dependent on the given atom and its local environment otherwise known as the crystalline electric field. If the local crystalline electric field has a low symmetry and the electric field of the bonding electrons is asymmetric then the atomic orbitals will interact anisotropically with the crystal field. Therefore certain orientations for the magnetic moment spins are preferred [18].

Figure 7 shows the magnetisation curves measured along the <100>, <110> and <111> axis of a BCC cubic crystal such as CoFe. In the <100> direction the predominant mechanism of magnetisation is domain wall movement. This requires a small amount of energy as can be seen by the small fields of under 100Oe required to saturate the material. This is known as the easy axis. In the <110> and <111> the mechanisms of magnetisation involve the shifting of domain walls until two domains of equal potential energy remain. After this saturation is achieved through the rotation of the M_s vector in each domain until parallel with the field. This domain rotation requires a significant amount of energy as can be seen from the 350-600Oe required to saturate the material. This is because in order to rotate the spins within the domains the spin-orbit coupling must be overcome. This is

known as the magneto-crystalline anisotropy energy which in cubic crystals such as CoFe and IrMn is expressed as [13]

$$E = K_0 + K_1(\alpha_1^2\alpha_2^2 + \alpha_2^2\alpha_3^2 + \alpha_3^2\alpha_1^2) + K_2(\alpha_1^2\alpha_2^2\alpha_3^2) + \cdots \quad (10)$$

where α_1, α_2 and α_3 are the cosines of the angles M_s makes with the crystal axes and K_0, K_1 and K_2 are the anisotropy constants for a specific material in ergs/cc. In the case of a uniaxial crystal such as that of single crystal Co the anisotropy depends solely on a single angle and becomes

$$E = K_0' + K_1' \sin^2\theta + K_2' \sin^4\theta + \cdots \quad (11)$$

where θ is the angle between M_s and the c axis. Due to the $\sin^4\theta$ dependence the third terms is negligible. In this study the magneto-crystalline anisotropy is the principle characteristic.

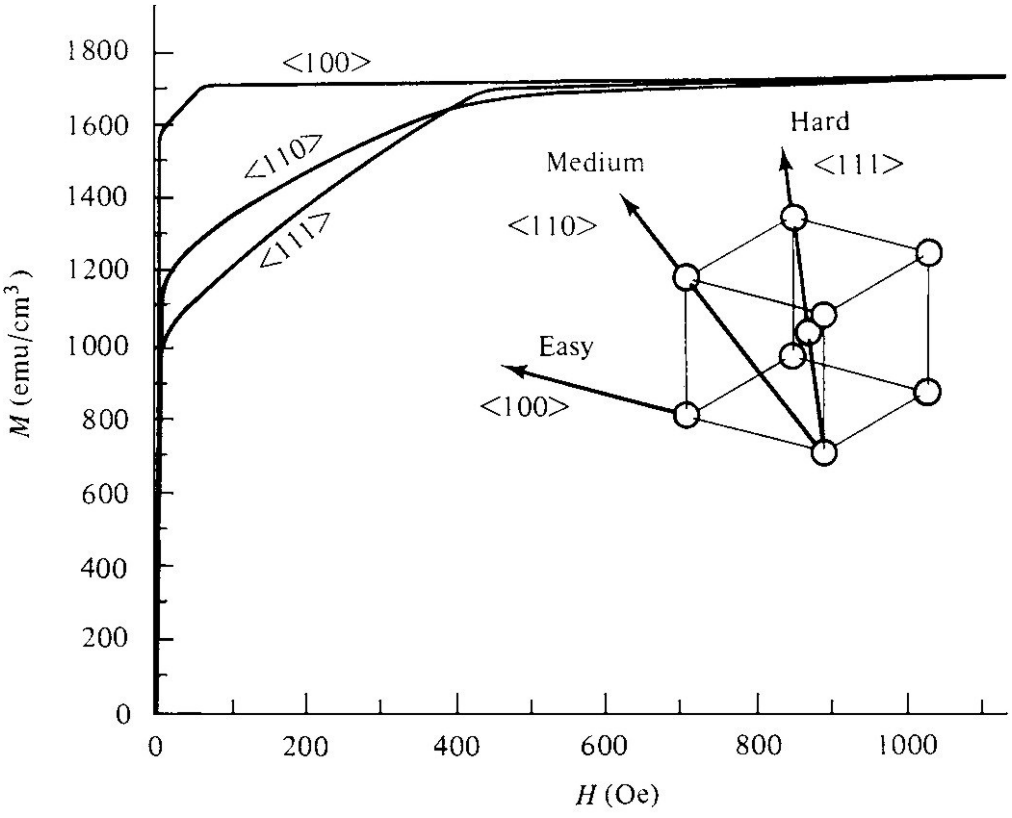

Figure 7: Magnetisation curves for a BCC crystal [13].

2.3.2. Shape Anisotropy

Anisotropy is also introduced into the system because of the geometry of the sample. This arises due to free poles of the outer surface creating a field H_D that opposes the magnetisation of the sample. This demagnetising field is proportional and in opposition to the magnetisation as described by

$$H_D = -N_D M \tag{12}$$

where N_D is the demagnetising factor which is geometry dependant. The demagnetising field is also inversely proportional to the separation of the free poles. In the case of the minor axis of a rectangular prism the pole distance is small and therefore the H_D is large. A greater field is then required to magnetise the sample along the minor axis as compared to the major axis where the pole distance is large. Shape anisotropy is negligible in the case of the polycrystalline films used in this study as the exchange interaction is the dominating factor. Surface roughness and edge effects which can lead to non-uniform demagnetising effects are present, however, which can alter the reversal process [13].

2.4. Antiferromagnetism

Antiferromagnetism plays an integral role in exchange bias and an understanding of the underlying mechanics is vital. Initially thought to be anomalous paramagnets, further study showed the uniqueness of their magnetic structure. In 1932 Néel [19] developed the theory of exchange bias in which Weiss's molecular theory was applied.

The susceptibility (χ) of an AF increases with temperature up to a critical temperature, known as the Néel temperature (T_N), and then decreases as in the case of a paramagnet. As can be seen in figure 8 the equation that describes this behaviour is that of the Curie-Weiss law however with a negative value of θ [13]

$$\chi = \frac{C}{T+\theta} \tag{13}$$

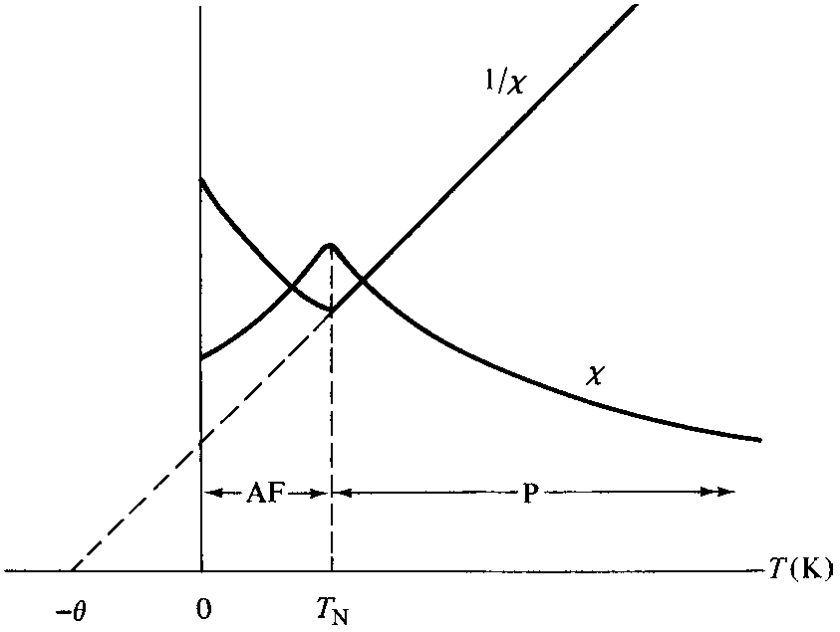

Figure 8: Schematic of the temperature dependence of the susceptibility χ and inverse susceptibility 1/χ for an antiferromagnet [13]. AF: Antiferromagnetic P: Paramagnetic

In the paramagnetic region as θ is proportional to the molecular field coefficient γ (see equation (3)) the molecular field H_m is opposed to the applied field H which leads to the misalignment of the magnetic moments. This results in the tendency for moments to align antiparallel to the adjacent moments which is represented by a negative sign on the exchange force. Below T_N this tendency towards an antiparallel alignment of the moments is strong enough to overcome random thermal energies. As such the lattice of magnetic moments breaks up into two ferromagnetic sub lattices of equal and opposite moment. These sub lattices align along some important crystallographic axis labelled as D in figure 9. It is the magneto-crystalline anisotropy that binds the spins to this specific axis and when applying high fields two effects can be observed: Spin Flopping and Metamagnetism [13].

In an AF material $\chi_\perp$ is greater than $\chi_\parallel$ when below T_N and so the state with spins at right angles to H is of lower energy. Counteracting this however is the magneto-crystalline anisotropy which binds the spins in the directions of the D axis. At some critical field the anisotropy is overcome resulting in a ‘flop’ of the spins from parallel alignment along D to perpendicular. This is shown schematically in figure 9(a) and 9(b). Metamagnetism occurs when the crystalline anisotropy is very strong which results in position (b) being unstable. As such the spins flop into

parallel alignment as shown in position (c) resulting in saturation of the material [13].

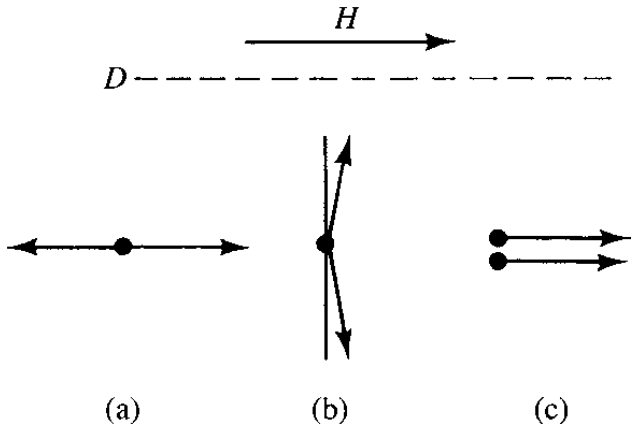

Figure 9: Schematic of Spin Flopping and Metamagnetism [13].

Chapter 3. Theoretical Models of Exchange Bias

The first model to attempt to explain the effect of exchange bias was that of Meiklejohn and Bean who discovered the effect in 1956 [1]. 10nm single domain Co particles with CoO oxide shells were considered. The interface was assumed to be perfectly flat with the interfacial AF moments being uncompensated by the interfacial F Moments. This led, however, to values of H_{ex} two orders of magnitude larger than those observed. Chronologically the second model proposed was that of Néel [20]. An uncompensated interface was again assumed, however interfacial roughness was added leading to partial compensation of the AF moments. This model also failed to correctly predict reasonable values of H_{ex}. These results were expected however due to the application of flat interfaces on round particles which is clearly not the case.

One of the more successful early models was that of Fulcomer and Charap [21] [22]. Their model was designed to explain their results of oxidised NiFe thin films and was the first granular model of exchange bias.

Mauri et al. [23] proposed the first domain model in 1987. It was suggested that domain walls formed parallel to the F/AF interface in order to lower the interfacial energy predicted by Meiklejohn and Bean. This model fails to explain, however, features such as an enhanced coercivity (H_C) of the F layer and reduction of H_{ex} upon field cycling. It also relied on an AF layer thick enough to accommodate a domain wall parallel to the interface even though exchange bias has been demonstrated in layers a few atoms thick. Malozemoff [24] predicted values of H_{ex} the same order of magnitude as Mauri et al. [23] by utilizing a random interface roughness. Due to interfacial roughness compensated and uncompensated areas exert fields on the F interfacial spins. Between the magnetostatic energy of the fields and the anisotropy of the AF layer, domains form within the AF with walls perpendicular to the interface. This model fails to explain exchange bias for perfectly compensated interfaces.

Schulthess and Butler [25] solved the Landau-Lifshitz-Gilbert equation in 1999 in order to research the exchange coupling at the interface. They found that in the case of a perfectly flat interface spin-flop coupling does not lead to exchange bias

but an increase in H_C of the F layer. Through the introduction of defects at the interface values of H_{ex} are obtained to the correct order of magnitude. This model applies, however, to the idealised case of single crystal and domain F/AF layers.

The domain state model was first proposed by Nowak et al. [26] in 2002. In the model the F layer is coupled to a diluted AF where the dilutions enter the system as non-magnetic atoms. Exchange bias arises in the system due to a domain state forming in the AF during field cooling and carries an irreversible magnetisation. The dilutions in the system favour the formation of the domain state with the assumption that domain walls preferentially pass through non-magnetic sites so as to reduce the energy needed to form them [27]. Although this model was dominant through the decade, it relied on the incorrect assumption that the AF anisotropy (K_{AF}) was infinite in order for the domain wall widths to equal zero. These models have all been reviewed in depth by O'Grady et al. [3].

3.1. Models of Exchange Bias

The following models merit further description due to their understanding of exchange bias as well as their contribution to the conceptual development of the York Model used in this study. Granular models of exchange bias are the only ones that are considered due to the polycrystalline nature of the samples used in this study.

3.1.1. The Model of Meiklejohn and Bean

Although not a granular model the work of Meiklejohn and Bean [1] is an important step in the general understanding of exchange bias. It was first proposed following their discovery of the exchange anisotropy in Co/CoO uniaxial single domain particles. These compacts were field cooled through T_N and their hysteresis loops measured. In their model it is assumed that the AF layer is fully uncompensated with only one AF sub-lattice in contact with the F layer at the interface. It is also assumed that the F layer rotates coherently. This is shown schematically in Figure 10.

Assuming that the F layers anisotropy is negligible and the condition $K_F t_F \ll K_{AF} t_{AF}$ is met the energy per unit area of the exchange bias system is given by [28]

$$E = -HM_S t_F \cos(\theta - \beta) + K_{AF} t_{AF} (\sin \alpha)^2 - J_{INT} \cos(\beta - \alpha) \qquad (14)$$

where J_{INT} is the interface coupling constant, H is the applied field, M_S and t_F are the saturation magnetisation and thickness of the F layer respectively, K_{AF} and t_{AF} are the anisotropy and thickness of the AF layer respectively. The angles α, β and θ are the angles between the AF sub-lattice magnetisation and easy axis, between the F layer magnetisation and easy axis and between the applied field and F layer easy axis respectively.

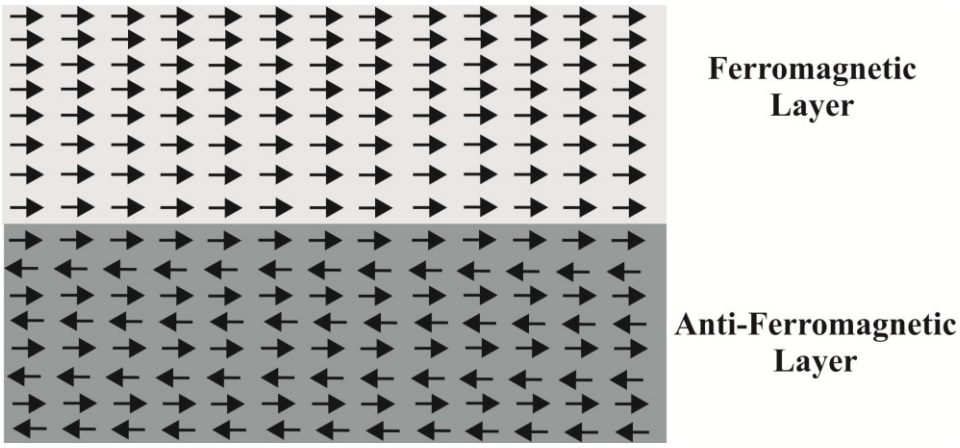

Figure 10: Schematic diagram of a fully uncompensated interface in an exchange biased system.

If the energy in equation (14) is minimised with respect to α and β a $\sin\theta$ shaped torque curve is predicted and an expression for the loop shift H_{ex} is given as

$$H_{ex} = \frac{J_{INT}}{M_S \cdot t_F} \qquad (15)$$

This model and equation (15) rely on a number of assumptions. Firstly it assumes that the interactions that give rise to the exchange bias are homogeneous throughout the sample. Secondly it is assumed that the applied field has a negligible effect on the AF in comparison to the exchange interaction with the F layer as described by J_{INT}. Thirdly in order for the AF grains to remain static as the F layer is reversed it is necessary for K_{AF} to be far greater than the exchange interaction from the F layer. Without this final condition there would be no shift measured in the hysteresis loop [29].

Although this model successfully describes some of the features of exchange bias there are some major flaws. If a value of J_{INT} similar to that of the exchange

interactions in F alloys is used in equation (15) it predicts values for H_{ex} several orders of magnitude larger then measured values [30]. The large rotational hysteresis found for exchange biased systems that remains constant at high fields is also not predicted. The rotational hysteresis suggests that some of the AF spins switch as the magnetisation is rotated. This is incompatible with the model as this situation leads to a zero loop shift. This model also fails to predict the reduction in H_{ex} and H_C as repeat hysteresis loops are taken on the same sample. Finally this model fails to predict time dependent irreversible changes in the AF layer [31].

3.1.2. The Model of Fulcomer and Charap

The first true granular model of exchange bias was the 'Thermal Fluctuation Aftereffect Model' of Fulcomer and Charap [21]. It was developed in an attempt to explain the temperature and measured frequency dependence of exchange bias observed for oxidised NiFe thin films [22]. In the model the AF is assumed to be an assembly of small non-interacting particles exchange coupled to the attached F layer. The total energy E_{AF} for a single particle is given by

$$E_{AF} = K_{AF} a_{AF} t_{AF} (\sin(\theta - \psi))^2 - J_{INT} c a_{AF} \cdot \cos(\theta - \phi) \qquad (16)$$

where θ, ϕ and ψ are the angle between the AF surface moment and the F easy axis, the angle between the magnetisation and easy axis of the F layer and the angle between the AF and F easy axis respectively. K_{AF}, a_{AF} and t_{AF} are the uniaxial anisotropy and area of the AF grain in contact with the F layer and thickness of the AF layer respectively. J_{INT} and c are the interface coupling constant and contact fraction. Due to the fact that two grains of equal area can have unequal surface moments c is introduced. When the F layer is reversed the coupling energy given by: $-J_{INT} c a_{AF} \cdot \cos(\theta - \phi)$ in equation (16) changes sign. The non-interacting AF grains then thermally switch over the energy barrier to reversal ΔE via a process similar to that of a Stoner-Wohlfarth particle. In polycrystalline and other granular materials there is a wide distribution of grain shapes and sizes which therefore gives rise to a large range of anisotropy (e_a) and coupling (Δe) energies. Fulcomer and Charap took this into account and derived an equation describing H_{ex} [21].

$$H_{ex} = \pm H_C - (N/M_S V_F) \int_0^\infty \int_0^\infty m(t) \Delta e G(e_a, \Delta e) de_a d\Delta e \qquad (17)$$

where N is the number of AF particles, *m(t)* is the time dependent surface moment of the AF layer and V_F and M_S are the volume and saturation magnetisation of the F layer respectively. Thermal activation is introduced into the model via *m(t)* as the surface moment of the AF is dependent on the orientation of the spins within the AF layer. The function $G(e_a, \Delta e)$ is the joint distribution function and is calculated by formulating it in terms of the grain area, thickness and contact fraction. These are all independent of each other and are related to the structure of the F and AF materials.

This model was able to successfully predict the general features of the temperature dependence of H_{ex} in Co/CoO and oxidised NiFe exchange biased systems however failed to predict the features of H_C. The theoretical fit to the experimental data in the case of Co/CoO is shown in figure 11.

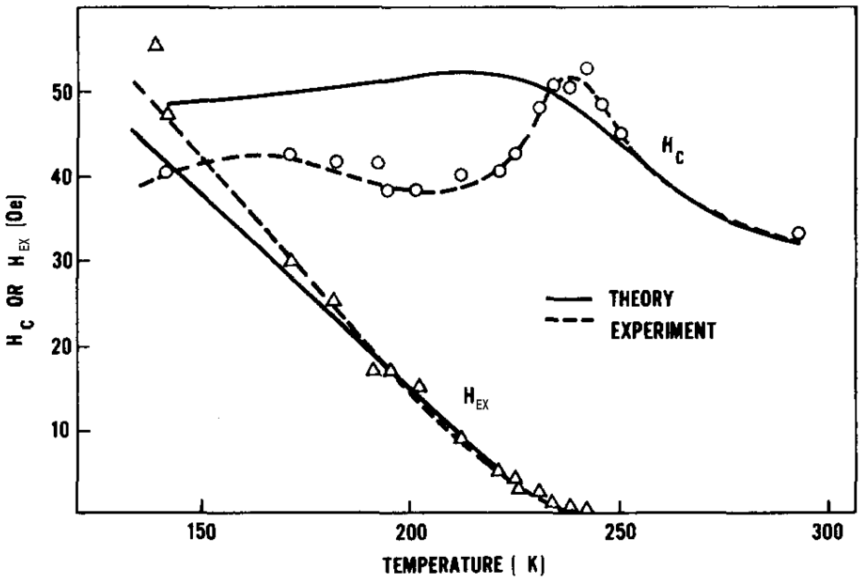

Figure 11: A graph comparing the theoretically predicted variation of Hex and Hc with respect to temperature with experimental data from Co/CoO exchange biased system [22].

Although the theoretical fit in figure 11 is relatively good in the case of H_{ex} it should be taken into account that the samples would have been thermally active during measurement. As such the values of H_{ex} and H_C would have been non-reproducible. This is due to thermal instability within the samples leading to a large, irreproducible, experimental error.

3.1.3. The Measurements of van der Heijden et al.

Van der Heijden et al. [32] made a series of measurements in which H_{ex} was measured as a function of time at a constant temperature. Samples utilising FeMn and NiO as the AF were produced via sputtering. Observations using TEM showed that the samples were both polycrystalline and displayed columnar growth. The samples were annealed at 500K and field cooled to room temperature.

To measure the time dependence of H_{ex} the sample was heated to the desired temperature whilst applying a field sufficient to saturate the F layer. The magnetic field was then set to reverse saturation and H_{ex} was measured as a function of time for which the field was measured using a magneto-optical Kerr effect (MOKE) magnetometer. The results in the case of NiO are shown in figure 12. As can be seen H_{ex} decreased with time and at higher temperatures was found to even change signs. When the field was reversed the opposite occurred. Van der Heijden et al. modelled their system as a distribution of single domain AF particles and achieved very good fits. Upon re-plotting of the results it is clear that there is a *ln t* dependence on reversal. However this was not considered in the original work of van der Heijden et al. [32].

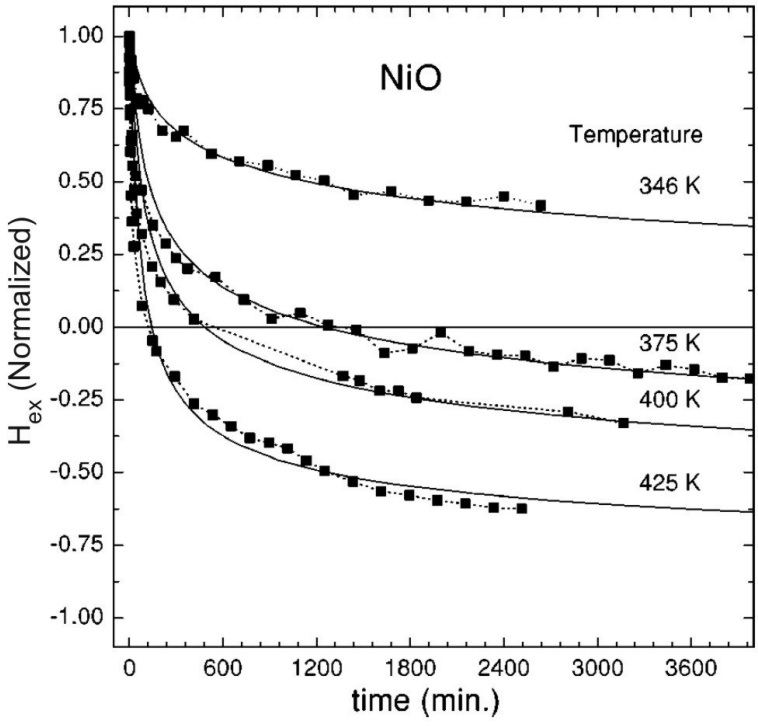

Figure 12: Data from van der Heijden et al. showing the time dependence of H_{ex} [32].

3.2. The York Model of Exchange Bias

The York Model was the subject of a recent review of exchange bias by O'Grady [3] et al. The model was developed in order to gain an understanding of the relationship between grain size, time dependence and temperature dependence of exchange bias. The York Model is applicable to polycrystalline thin films with an average grain diameter in the range of 5nm – 20nm. A recent addition to the model allows it to be expanded to the case of multi-domain and single crystal samples. This is because the addition of impurities to the system causes domain wall formation and pinning. As impurities are added the size of the domains decrease until they are of equivalent size to that of a single domain grain at which point they align through rotation [33]. As such it is based on the granular model of Fulcomer and Charap [21]. In the York Model the AF grains are shown to be non-interacting and a layer of disordered spin clusters is shown to exist at the interface.

3.2.1. The Behaviour of the Bulk of the AF

In the York Model the AF is shown to be made up of a distribution of non-interacting single domain grains where the energy barrier to reversal of an AF grain ΔE is

$$\Delta E = K_{AF} V_{AF} \left(1 - \frac{H^*}{H_K^*}\right)^2 \tag{18}$$

where K_{AF} and V_{AF} are the anisotropy constant and volume of the AF grain. The value of K_{AF} is found to be constant however it may vary from grain to grain due to compositional inhomogeneity or structural defects. H^* is the exchange field from the F layer and H_K^* is a pseudo anisotropy field similar to that of the anisotropy field in the F layer.

Due to the difficulty in setting thin films at the Néel temperature of IrMn, taken to be 690K [34], it is necessary to use thermal activation. This is carried out by applying a saturating field along the easy axis of the F layer and applying a temperature below T_N. The relaxation time of an AF grain being set is given by

$$\tau^{-1} = f_0 exp\left[-\frac{\Delta E}{k_B T}\right] \tag{19}$$

The AF grain volumes follow a lognormal distribution as shown in figure 6. The grain volume distribution is calculated by measuring the lateral grain diameter and then assuming a columnar grain structure. As can be seen in the experimentally obtained data in figure 13 a wide distribution of grain volumes can be obtained through variation of the system properties. From equation (18) this will lead to a wide distribution of energy barriers throughout the AF [3].

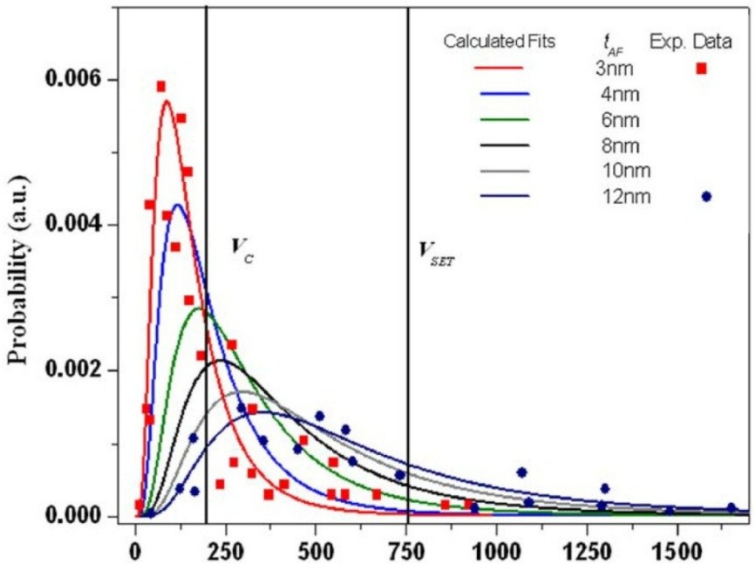

Figure 13: Graph showing the measured grain volume distributions for different AF layer thicknesses [3].

By equating and rearranging equations (18) and (19), for a given setting temperature T_{set} and a given time t_{set} the volume of the largest grain that can be set is given by

$$V_{set} = \frac{k_B T_{set} \ln(f_0 \cdot t_{set})}{K_{AF}(T_{set})} \tag{20}$$

where $K_{AF}(T_{set})$ is the AF layer anisotropy at T_{set}. The term H^*/H_K^* is neglected as it has been shown to be small when the ferromagnetic layer has a thickness of less than 5nm [35]. When a sample is measured at a given temperature T_{meas} there is a possibility that a certain fraction of the grain size distribution below a certain critical volume V_C will be thermally unstable. This volume is given by

$$V_C = \frac{k_B T_{meas} \ln(f_0 \cdot t_{meas})}{K_{AF}(T_{meas})} \tag{21}$$

where the anisotropy constant at T_{meas} is $K_{AF}(T_{meas})$ and t_{meas} is the time taken to complete the measurement. The AF grains that then contribute towards the value of H_{ex} are those that are stable at T_{meas} over the time t_{meas} and that were set when heated to T_{set} for the time t_{set}. As such H_{ex} can be modelled as being proportional to the integral of the grain volume between the limits of V_{set} and V_C [3]

$$H_{ex}(T_{ms}) \propto \int_{V_C}^{V_{set}} V f(V) dV \tag{22}$$

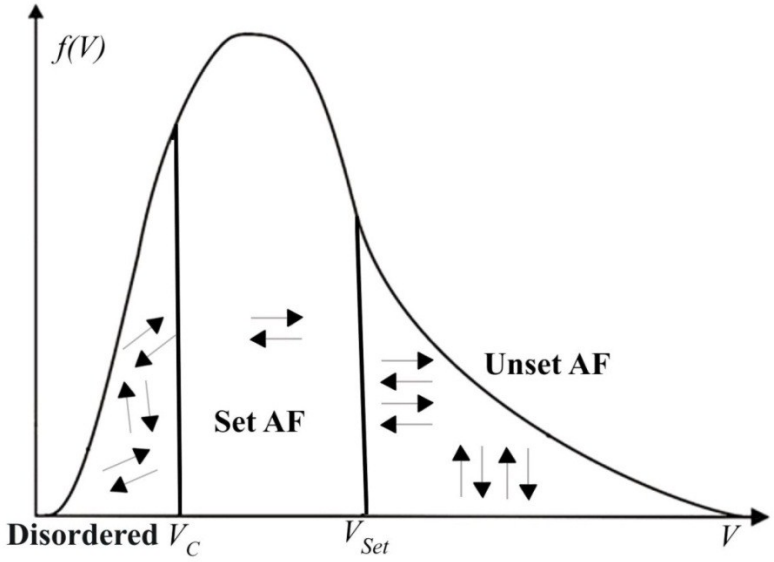

Figure 14: Schematic showing the disordered, set and unset portions of the AF grain volume distribution [3].

As shown schematically in Figure 14 only the grains within the limits $V_C < V < V_{set}$ will contribute to H_{ex}. As the grain volume distribution in sputtered thin films is both log-normal and highly asymmetric, as can be clearly seen in figure 13, any changes to the grain size or layer thickness will produce non-linear variations in H_{ex}. Results demonstrating this are shown in figure 15 a) and b). Equation (22) was used to fit these results using a scaling factor C^* which represents the strength of the interfacial coupling. This factor affects the magnitude of the values of H_{ex} along the axis and does not affect the shape of the curve. The ability of the theory to fit the shape of the results, within error, confirms the validity of this description of the bulk AF properties.

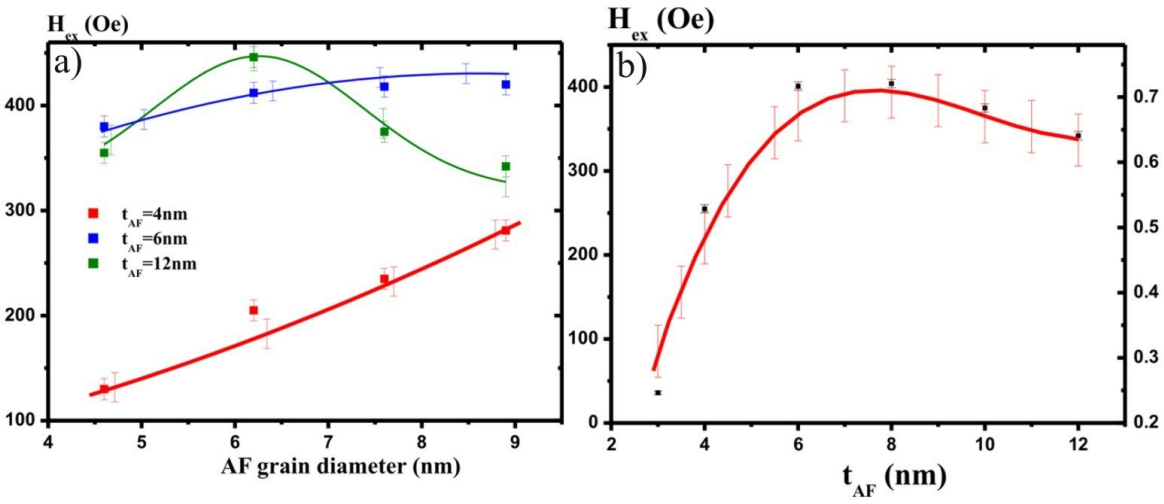

Figure 15: Results (points) and theoretical calculations (solid lines) from equation (23) (using equations (21) and (22) with K_{AF} measured using equation (36) and measured values of $f(V)$) showing: a) the variations in H_{ex} with respect to AF grains diameter. b) the variation in H_{ex} with respect to the AF layer thickness [3].

3.2.2. The Behaviour of the Interface of the F/AF

It has been shown that when the setting field H_{set} is increased from 1kOe to 20kOe the value of H_{ex} can increase up to 20% [36]. As CoFe saturates at ~350Oe this increase is not due to magnetic ordering in the F layer. This result is shown in figure 16a) where the increase in H_{set} is shown for two different F layer thicknesses. A large variation in H_{ex} is observed however when compared to T_B measurements in figure16b) no change in the distributions is observed. This clearly shows that the increase in H_{set} is not due to variations on the bulk but in the interfacial ordering. The value of H_{ex} measured can therefore not be solely dependent on the ordering of the bulk of the AF and has an interfacial component.

This gives the equation

$$H_{ex}(T_{meas}) = H_{ex}^{i} C^{*}(H_{set}, T_{set}) \int_{V_C}^{V_{set}} V f(V)\, dV \qquad (23)$$

where H_{ex}^{i} is some intrinsic value of exchange bias for the system and $C^{*}(H_{set}, T_{set})$ is the strength of the interfacial coupling. The strength of the interfacial coupling is determined by the setting field and temperatures.

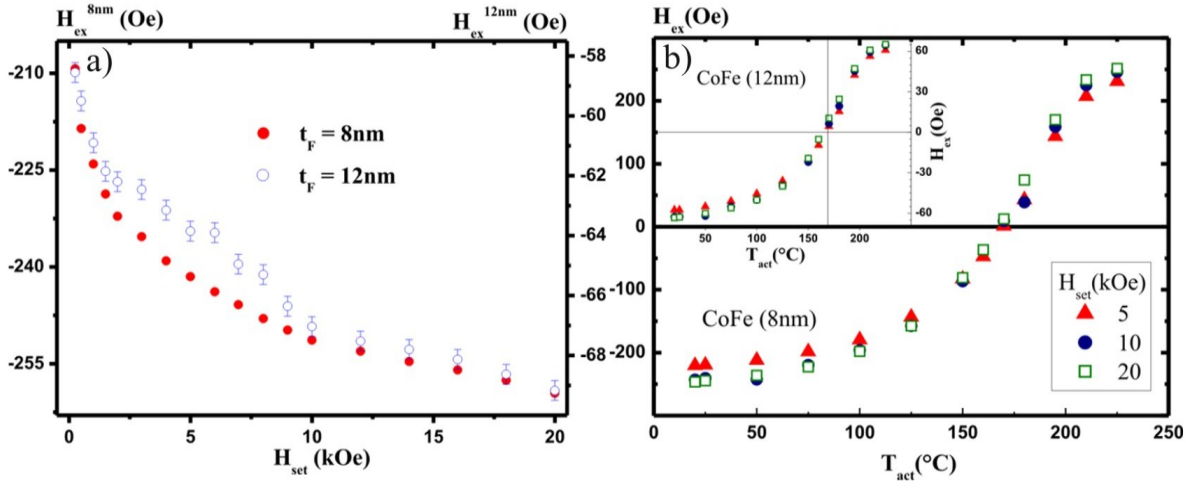

Figure 16: Graphs comparing the effect of 8 and 12nm thick CoFe layers on a) the change in H_{ex} with respect to the setting field and b) the blocking temperature distribution [3].

Although this model is capable of making accurate predictions of the value of H_{ex} with respect to a number of variables it cannot account for the thermal training effect. Hoffman [37] theorised that the training effect occurred due to spin-flop coupling established at the F/AF interface. Upon the F layer becoming reversed the AF spin structure changes from a biaxial to uniaxial orientation resulting in a decrease in H_c from that observed in the initial loop. Recent work within the York group [4] has provided substantial evidence for a different origin of training as well as insight into the nature of the F/AF interface.

In the work a tri-layer system consisting of two F layers of different thickness separated by a thin AF layer was studied. With this system two hysteresis loops exchange biased to different degrees and separated by a plateau were obtained. As can be seen in figure 17b) the sample was measured over the first loop only (black line) and then over the full two loops twice (grey then dotted line). In comparing the three measurements it was seen that the first loop removed the training only in the hysteresis loop of the thicker F layer, F1. Only when both loops were measured to negative saturation was it found that the training in the thinner layer, F2, was removed [4]. This implies that training is solely an interfacial effect and as the AF layer was only 4nm thick it implies that the interfacial spin structure cannot extend more than one or two atomic layers.

Using the York Protocols, which will be described in section 4.4, it is also possible to thermally activate one or both F layers. When the system is thermally activated

with moderate temperatures (<150°C) to a field sufficient to reverse only the thicker F layer a change in the loop shift for the thicker layer is observed. However there is no observable change, within error, in the loop shift of the thinner F layer. This result as shown in figure 17a) suggests only the interface between the F and AF layers is affected by the thermal activation process.

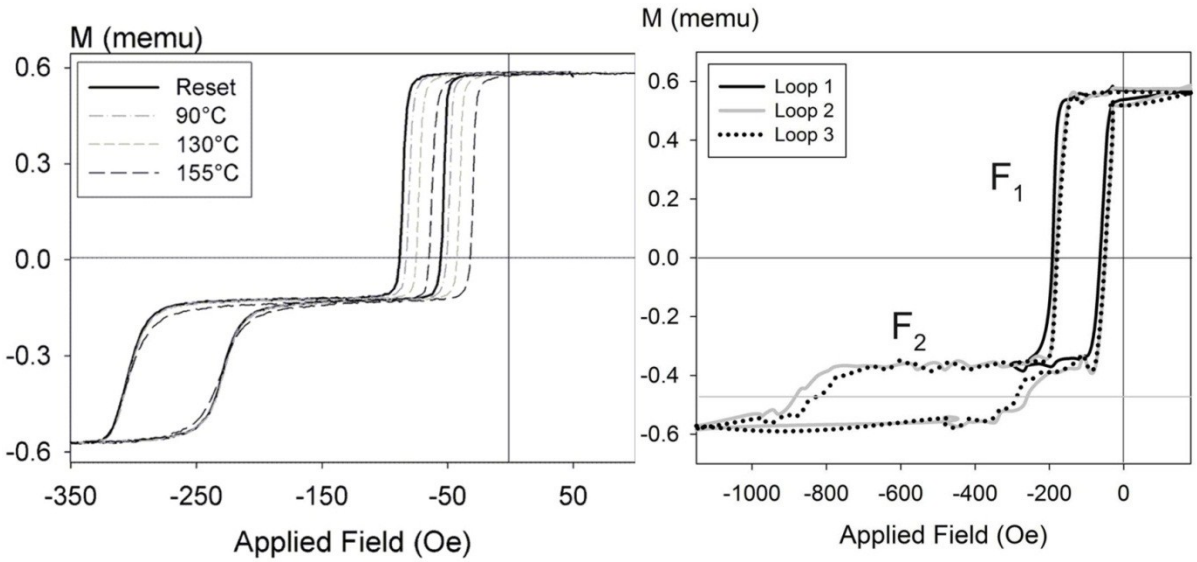

Figure 17: Trilayer results showing the effect of a) thermal activation of a single F layer [3] b) removing thermal training from a single F layer [4].

Considering these results it is thought that the interfacial spins behave as superparamagnetic clusters. The ordering of the spin clusters is thought to follow a Langevin function where α is assumed to be small. Therefore the magnetisation of the spin cluster will be proportion to its area

$$\frac{M}{M_S} = \frac{\alpha}{3} = \frac{N\mu_\beta\left(H_{set}+H_{int}^*\right)}{3kT} \tag{24}$$

where N is the number of spins in each cluster, μ_β is the Bohr magneton and H_{int}^* is the exchange field which the spins experience due to spin-spin interactions and F/AF layers. If H_{int}^* is taken to be 50% that of pure iron then the optimum fits for the variation H_{ex} with H_{set} are found when the interface spins exist in clusters of 10 to 50 spins [36]. This behaviour is similar to that observed in other spin cluster systems such as in the case of spin glasses which have been observed in AF systems [38]. However in this case the system is two dimensional as shown in figure 18.

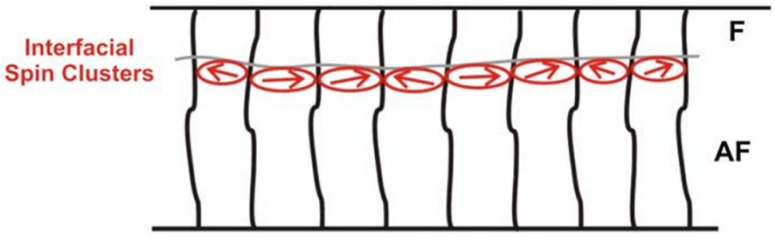

Figure 18: A schematic showing the assumed structure of a polycrystalline exchange biased system along with the location of the interface spins [3].

The underlying mechanism of the training effect is then due to the ordering of these interfacial spin clusters. When the sample is initially set and then field cooled a significant degree of coupling is induced between the clusters forming a relatively aligned magnetic structure. When the field is reversed it is thought that clusters possessing lower anisotropy, or not as strongly coupled via exchange and dipolar interactions to their neighbours, may lose their ordering. On returning the field to positive saturation these spin clusters lack the energy to realign into their original microstructure creating the observed training.

3.3. Compositional Effects of IrMn

The most commonly used exchange bias system in GMR/TMR read heads is $Ir_{20}Mn_{80}/Co_{35}Fe_{65}$ because it has been shown that the stoichiometry of the IrMn alloy has a strong effect on H_{ex}. It was found [34] that the ordered $L1_2$ phase of $IrMn_3$ results in a peak in H_{ex}. In order to control the atomic ordering of IrMn so as to obtain the $L1_2$ phase seed layers must be used and the composition of the layer must be controlled.

In 2006 Tsunoda et al. studied the effects of Ir composition, seed layer and substrate temperature on the degree of order (S) and the uniaxial anisotropy J_k of an IrMn/CoFe system [34]. A peak and plateau in H_{ex} was found for 22-32% Ir which corresponded to the formation of the $L1_2$ phase. From the seed layers studied it was also found that Ru gave the best texturing. In 2010 [39] [40] similar experiments were carried out using the York Protocols. The effect of both seed layers and composition on the blocking temperature distribution and AF anisotropy were investigated. A similar result to Tsunoda et al. was found with a plateau in H_{ex} being measured in the range 13-22%. An increasing linear relationship was found, however, for K_{AF} as Ir content was decreased. It is likely that as the Ir

concentration was reduced the $L1_2$ ordering developed in some, but not all, of the AF grains due to the composition not being uniform. This could explain the difference in trends between H_{ex} and K_{AF}. These results are shown in figure 19.

The interfacial coupling also determines the value of H_{ex}. The spin structure at the interface has been shown to be highly dependent on composition [41]. Tsunoda et al. showed that uncompensated Mn moments exist at the interface between the CoFe/IrMn layers [42]. These uncompensated spins arise due to the exchange interaction between the Mn and CoFe. Recently it was found that through the exchange interaction the Mn spins at the interface try to align parallel to the Co moments but antiparallel to the Fe moments [43]. Therefore the induce Mn moments are different from point to point and rely on the local environment of the Mn atoms and the neighbouring F atoms. The local rotations of the Mn moments will then affect the spin structure within the AF layer.

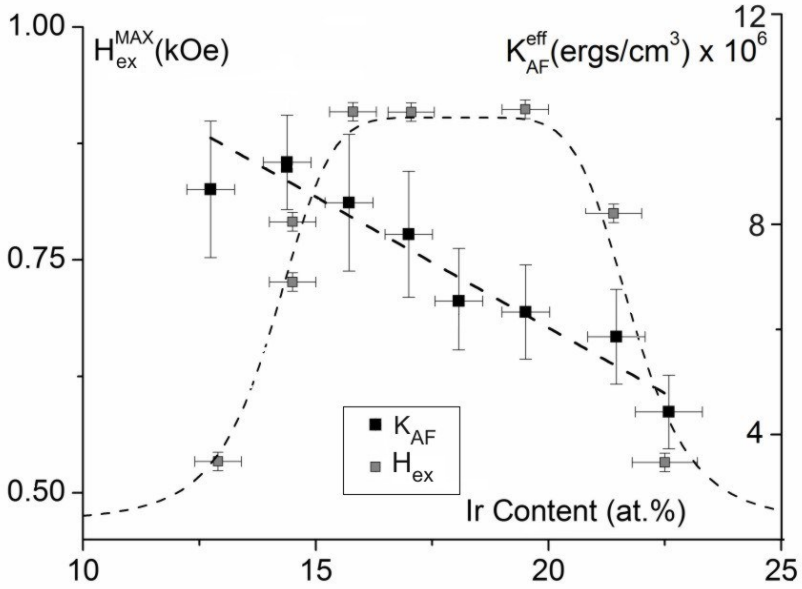

Figure 19: Graph showing the measured variation in both anisotropy (Kaf) and loop shift (Hex) with respect to Ir content [40].

Tsunoda et al. found that by inserting 0.5nm of Mn at the interface of a CoFe/IrMn bilayer an increase in H_{ex} of ~50% is observed [44]. They concluded that the enhancement was most likely due to the modification of the AF spin structure at the interface.

3.4. Other Models

There are many other models of exchange bias which have been developed especially since the wide scale availability of large scale computing capabilities. Some of these models e.g. the Domain State Model [26], the Coupled Granular Model and Finite Element Models [45] [46] [47] have had limited success in predicting a selection of observed phenomenon in exchange biased systems. However the York Model is the only comprehensive model that can explain all facets of the behaviour of the bulk of the AF grains and, at least at a phenomenological level, effects at the interface between F and AF layers.

Furthermore no model other than the York Model can simultaneously explain the film thickness dependence of H_{ex}, the lateral grain size dependence of H_{ex} and the setting rate dependence. The model is also predictive rather that providing a fit to data using floating parameters.

Chapter 4. Methodology

4.1. Sample Preparation

Magnetic materials are a major area of research with applications that range from the fundamentals of physics to the application and development of new commercial products and processes. In the case of magnetic thin films there are three predominant methods of sample production each with different system properties.

The first of these methods is Molecular Beam Epitaxy, or MBE. It functions by evaporating the wanted material from a high purity target in an Ultra High Vacuum (UHV). A UHV in an MBE system is generally defined as $<x10^{-10}$ mbar and it is required for a sufficiently large mean free path of the evaporated atoms. The vaporised material traverses the chamber and condenses onto a single crystal substrate. For fully epitaxial single crystal growth there must be sufficient lattice matching at the interfaces otherwise stress accumulates in the growing layer causing fractures. MBE has the advantage of having atomically flat interfaces consisting of at most atomic steps. Growth rates are low, however, at <0.25nm/s. Accurate sample growth from alloy targets is difficult due to differences in evaporation rates of the materials used. As such MBE is generally used to create multilayers from single metal targets [48].

The second of these methods is sputtering. In sputtering a plasma is used to bombard a high purity target. Through the transfer of kinetic energy the impinging ions eject atoms of the material ballistically from the surface. For non-reactive sputtering Ar plasma tends to be used due to both the large atomic mass of Ar and its relatively low cost. In sputtering the plasma is formed by filling a vacuum chamber with Ar and then applying a high voltage to the target. The large electric field ionises the Ar and causes the Ar^+ ions to collide with the target. This creates secondary electrons, which continue to ionise further atoms, and eject the material. This process provides extremely slow sputter rates of less than 0.1nm/s. Through the addition of a magnet below the target the secondary electrons can be used to create a ring of high intensity plasma above the surface of the target increasing sputter rates by up to an order of magnitude [49]. Due to the comparatively high growth rates of greater than 1nm/s this process is the most

prevalent in industry. The ability to sputter polycrystalline materials from alloys and to control the size of the grains through seed layers has made this method the ideal choice for the HDD industry in particular.

The final common method of growth is ion beam sputtering (IBS). With IBS an external ion source, commonly Ar, is used to bombard the surface of a target. Much like sputtering, alloy targets can be used and the material grown is polycrystalline, however due to low growth rates of <0.25nm/s grain sizes tend to be very small. As such IBS is generally used in multilayer systems in the production of HDD read heads.

4.1.1. High Target Utilisation Sputtering

Although magnetron sputtering is widely used in industry there are a number of inefficiencies within the system. First of all is the location of the generated plasma. As mentioned previously the applied magnetic field generates a ring of plasma above the surface of the target. Due to the much higher sputter rates caused by this plasma a ring, or racetrack, is cut into the target whilst the rest is contaminated. A second problem is that as a magnet is required under the target if a F material is used the field is modified to the point that efficient sputtering no longer occurs. The High Target Utilisation Sputtering system (HiTUS) corrects for these problems by generating the plasma in a sidearm [50].

The plasma, Ar in this case, is generated by applying a 0-2.5kW RF field across the Ar gas in the side arm. The plasma is then drawn into the chamber through interaction of the RF field with the launch electromagnet. This plasma is drawn towards the target using the steering electromagnet. This occurs due to the electrons following chiral paths along the field lines generated by the launch electromagnet. As they traverse these paths the electron gain enough energy to ionise further Ar atoms in the path seen in Figure 20. This gives the effect of the plasma being drawn into the growth chamber. A similar effect is then responsible for the steering of the plasma onto the target. A 0 – -1000V DC bias voltage can then be applied to the target. This bias voltage is not required to generate the plasma however it is required for sputtering to occur. Above -100V the target current saturates and becomes independent of the voltage. It is then possible to

vary the energy of the Ar^+ ions, and therefore the deposition rate, without altering the plasma density. A schematic of the HiTUS system is shown in Figure 20.

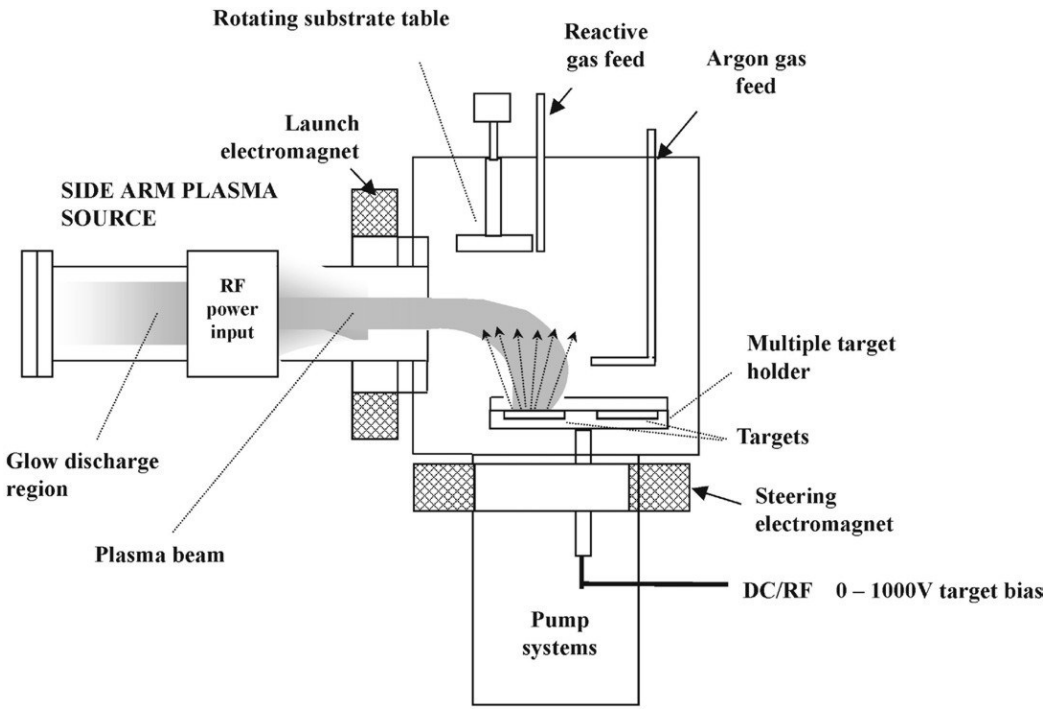

Figure 20: Schematic drawing of the High Target Utilisation Sputtering (HiTUS) growth device [51].

One of the benefits of this system is that the area of the plasma covers the whole surface of the target and a racetrack does not form. Figure 21a shows an example of the target utilisation and as can be seen >90% of the target shows even wear. As there is equal sputtering across the sample it is then possible to vary the composition of the sputter target. This is done by inserting pins of other materials into holes drilled into a specially designed target as shown in Figure 21b [52].

A second benefit is that no magnetic field is required for the formation of the plasma and so sputtering from thick F targets is possible. More importantly, however, is that the properties of the plasma can be very simply altered by varying three controls: The Ar gas pressure, RF field power and finally the target bias voltage. This allows for very simple control of deposition rate from 0.1 to 2.0 nm/s and, therefore, median grain size from under 5 to 25nm [51].

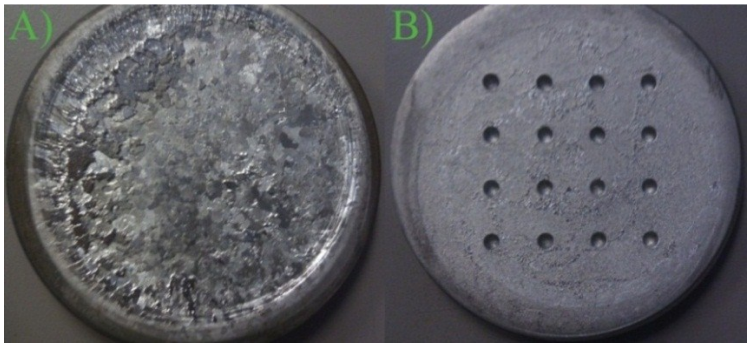

Figure 21: Examples of a) >90% target erosion and b) composite target for varying IrMn composition.

Due to the construction of the system up to 8 targets and 6 substrates can be used without breaking vacuum. Also due to the relatively low growth temperatures from ambient to 200°C and crystal formation without annealing Carbon coated Copper TEM grids can then be deposited on. As sputtering provides line of sight growth there is equal deposition rates for both the TEM grids and Si substrates as they are placed within 5 mm of each other above the target. The layer thickness is judged using a water cooled quartz crystal growth rate monitor also placed within 5 cm of the substrate position. This allows for accurate growth of single atomic layers on multiple substrate types for any one sample.

The growth of the grains is columnar and so through the use of seed layers specific crystallographic orientations may be obtained [39]. This allows for control over the anisotropy of the AF and therefore the systems thermal stability. Due to this as well as the ability for this system to control grain size it was used to grow all samples within this study.

4.2. Magnetic Measurements

For development of new magnetic materials to be possible an accurate understanding of their properties is required. A number of methods are available for the magnetic characterisation of a material. Closed coil systems such as a B-H loop tracer and AC susceptometer are useful for performing susceptibility and low-field hysteresis loop measurements. However in the case of exchange bias thin films large fields in the order of kOe are required both to saturate the ferromagnetic layer as well as to detect the offset loop. As such methods utilising open coil detection systems with large electromagnets such as the alternating

gradient field magnetometer (AGFM) and vibrating sample magnetometer (VSM) are required.

4.2.1. Alternating Gradient Magnetometer

The AGFM is an application of the force method. This operates by placing the magnetisable sample in a non-uniform magnetic field and then using the applied force to work out the magnetisation. The force felt by the sample when magnetisation is uniform through the sample and the field varies with position is given by

$$F_M = -V_S M \cdot \nabla B_0 = -m\sigma \cdot \nabla B_0 \tag{23}$$

where V_S and m are the volume and mass of the sample respectively. The field gradient is obtained either by shaping the poles or superimposing a field gradient produced by an electric current [53]. In an AGFM the sample is placed on a probe that consists of a glass sample holder attached to two quartz legs. The end of each quartz leg is then attached to opposite sides of a piezoelectric bimorph. The applied force is then detected by measuring the current generated by the bimorph. Although the noise base of this system is very low at $x10^{-8}$emu there are some important restrictions. The sample mass must be under 100mg and due to the sensitivity of the system temperature variations and acoustic noise can cause measurement shifts. As such the AGFM tends to be used for very high resolution hysteresis loops as well as measuring time dependence of samples.

4.2.2. Vibrating Sample Magnetometer

The final method takes advantage of the current induced when a magnetic dipole is moved through a coil. The flux ϕ_F produced by this dipole can be found by doing the time integral of the induced voltage $\int e\, dt$. If the coil is placed inside of a source of field the moment can be measured as a function of the externally applied field. The total flux is given by $\phi_F = \int B dS$ over the volume of the sample where dS is an element of area. So using

$$B = B_0 + M \tag{24}$$

if B_0 is known sufficiently accurately then the magnetisation can be directly calculated from ϕ. The magnetometer most commonly used that exploits this

method is the vibrating sample magnetometer (VSM). This functions by vibrating the sample between a set of pickup coils under an applied field generating an alternating signal within the pickup coils [53].

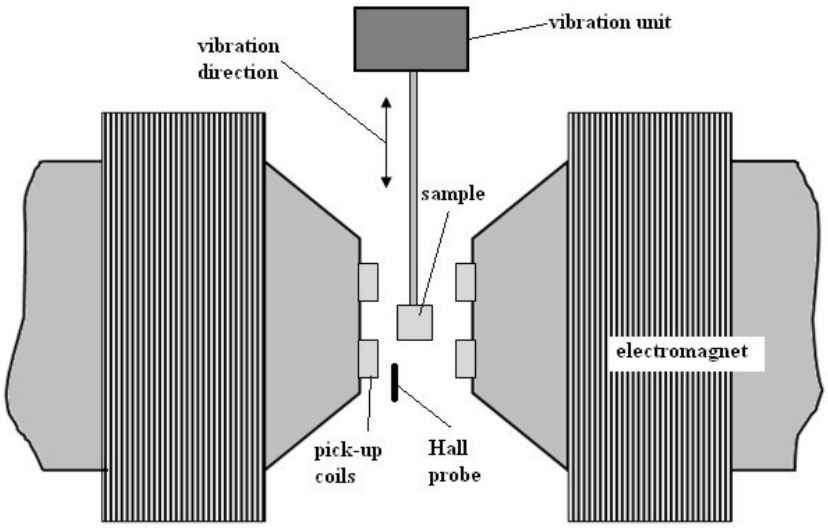

Figure 22: Schematic of a Vibrating Sample Magnetometer

The coil design of a VSM is of great importance if low noise measurements are to be obtained. In the case of older VSM design, such as that shown in figure 22, four detection coils are used and resistance matched to an accuracy of ± 0.025 ohms. Each coil pair is connected in series to eliminate noise produced due to stray fields. The coil pairs are also aligned so that their axes lie perpendicular to that of the magnetising field so as to not detect field fluctuations [53]. In more modern designs, such as the Microsense Model 10 VSM used in this study, an 8 coil design is used with their axes perpendicular to each other. This allows for measurements of the magnetisation to be measured as a function of angle. A measurement resolution of up to 1×10^{-6} emu may be obtained whilst using a 100ms time constant and taking ten averages per point.

The vibration of the sample is provided using a speaker driver set at ~81Hz. This is chosen so as to prevent mains driven noise. To account for any acoustic noise or variation in the driving signal a reference signal is generated at the top of the sample rod. A lock-in amplifier is then used to compare the amplitude difference between the reference signal and the signal detected by the pickup coils.

Due to the sturdy design of the VSM it is relatively immune to acoustic noise and external magnetic fields. This along with the fact that the temperature of measurements can easily be varied from 2.7K to >1000K means that very quick measurements can be made in a variety of conditions. This makes the VSM a powerful tool in the characterisation of materials such as magnetic thin films.

4.3. Grain Size Distribution

To obtain information on the grain size distribution TEM in-plane imaging of the sample is necessary. This is achieved by thinning a sample's substrate until it is electron transparent. In this study the samples have been deposited directly onto Cu TEM grids negating the need for sample thinning.

4.3.1. Transmission Electron Microscopy

The underlying physics of transmission electron microscopy (TEM) is analogous to that of optical transmission microscopy. By shining light through a thin enough material individual features can be resolved due to changes in colour and opacity. However the visible spectrum consists of a range of wavelengths from 350-790nm and so is restricted from observing smaller features. Using the de Broglie relationship

$$\lambda = \frac{h}{mv} \tag{25}$$

it is seen that the wavelength of kV energy electrons is picometer in scale. As such sub-Ångstrom imaging of materials is possible however the source of contrast is different to that of optical microscopy [54]. Electrons are strongly scattered through Coulomb interactions with the nucleus and atomic electrons. Contrast is therefore dominated by the atomic and crystallographic properties of the material. There are two sources of amplitude contrast in TEM imaging. The first is the mass-thickness contrast. As the cross section for elastic scattering is a function of Z high-Z regions of a sample will scatter more electrons than that of low-Z regions. Similarly as the mean-free path of an electron is fixed in a material with a single Z value a thicker material will elastically scatter more electrons. This form of contrast mostly dominates for non-crystalline materials such as biological

specimens [55]. The second is diffraction contrast. Bragg diffraction as defined by (26) is controlled by the crystal structure and orientation of the sample.

$$n\lambda = 2\mathrm{d}\sin\theta \tag{26}$$

Through coherent elastic scattering of the electrons a diffraction pattern is produced. Crystalline samples tend to give single crystal diffraction patterns. By using two-beam conditions it is possible to get a strong diffraction contrast for specific crystal orientations. This is achieved by tipping the sample so that only one diffracted beam is strong. By imaging this beam specific orientation information can be obtained as the electrons have been diffracted by a specific set of *hkl* planes. As the samples used in this study are poly-crystalline the diffraction pattern obtained is a superposition of multiple single crystal diffraction patterns [55].

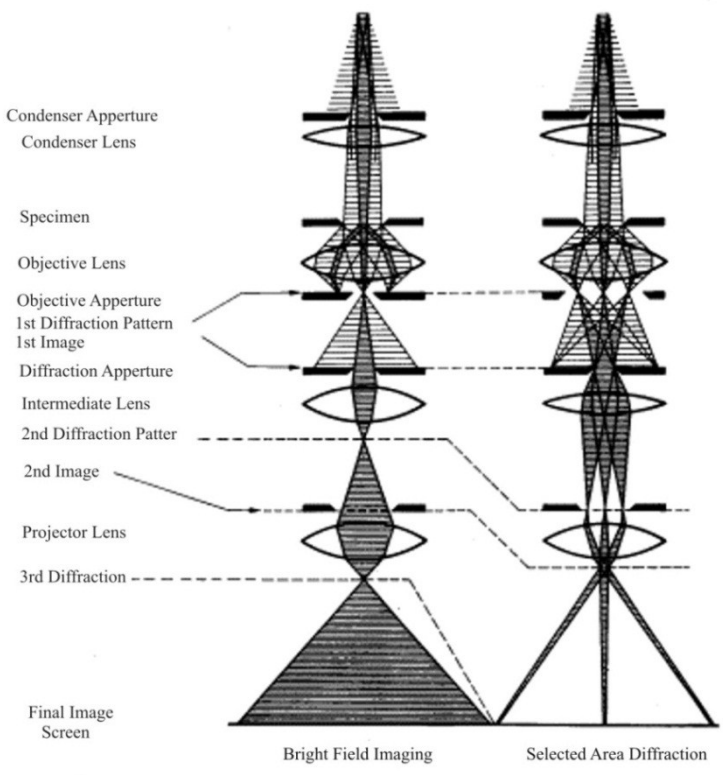

Figure 23: Transmission electron microscope ray diagram depicting both bright field imaging and diffraction mode demonstrating the different operation of each lens and aperture.

The electron beam in the JEOL 2011 TEM is generated using a thermionic emission gun. The area of the specimen which is sampled by the beam is varied using the condenser system. The beams diameter and convergence angle are controlled using the condenser lenses and aperture respectively. The specimen is placed onto a sample rod and entered into the system via an air lock on the side of the column. It is possible to move the sample rod up to 2mm in the x and y directions and 0.1mm in the z axis. This is used to navigate the sample and is stable to at least 0.1nm. In order to select whether the image or diffraction pattern is to be viewed the objective lens and aperture must be used. This is done by focusing on the image or back focal plane respectively. This forms the first intermediate image. Magnification of this image is controlled via a series of projector lenses. To achieve a magnification of x1000000 all that is required is three or four lenses set at x20. The resultant image is then displayed on a phosphorus screen at the bottom of the column and images are recorded using a CCD camera. A schematic of the system is shown in figure 23 in two operating modes [54].

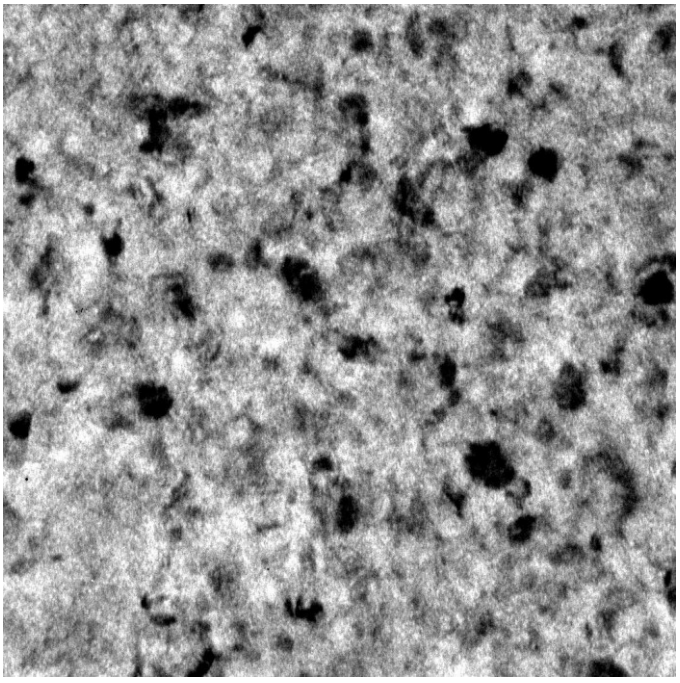

Figure 24: A typical bright field TEM image taken using a JEOL 2011 TEM.

For grain size analysis it is only the black grains that are counted as they are the electrons that perfectly fit the Bragg conditions. It is therefore beneficial to attempt to maximise the diffraction contrast. This can be done by removing contributions

from grains that do not perfectly fit the Bragg conditions by using the objective aperture. Ideally only the direct beam should be viewed however intensity loss is severe and the image obtained overlaps with the dark field. A typical image using this technique is displayed in figure 24. It is also possible to view the diffracted electrons. This gives an image analogous to a negative of the bright field however the grains seen are composed solely of electrons diffracted to the area selected. A far greater contrast is achieved in the dark field mode however information is lost and so bright field is preferred [55].

4.3.2. Grain Size Analysis

The grain size distribution is a critical parameter in the development of polycrystalline thin film devices. It has been shown that growth processes in granular systems follows a log normal distribution [56]. The log normal distribution is defined as

$$f(D)dD = \frac{1}{(\sqrt{2\pi})\sigma D} exp\left\{\frac{\left((\ln D)-\mu\right)^2}{2\sigma^2}\right\} dD \tag{27}$$

where D is the particle diameter, σ is the standard deviation of lnD and μ is its mean. The median diameter of the distribution is given by

$$D_m = e^{\mu} \tag{28}$$

where the median is defined as the measurement at which half the values are less than or equal to it and the other half are greater. The standard deviation of lnD for an n number of measurements is [56]

$$\sigma = \left[\frac{1}{n}\sum(\ln D)^2 - \left(\frac{1}{n}\sum \ln D\right)^2\right]^{1/2} \tag{29}$$

The grain size distributions were measured using a Zeiss particle size analyser which utilises an equivalent circle method. A TEM image of the grains is printed and placed on a light box. A brightly lit iris makes it possible to match an equivalent circle with that of the size of a grain within the image. This size is then recorded as 1 of 40 bins to which it corresponds. The Zeiss particle size analyser has been calibrated so that each bin records a specific diameter. By then using the scale on the image it is possible to obtain the grains sizes of the sample. A

minimum of 500 grains were measured in this study as it has been shown that this is the number required to characterise the distribution correctly [56]. Figure 25 demonstrates the quality of fit achieved using the aforementioned methods when n≥500 grains have been measured.

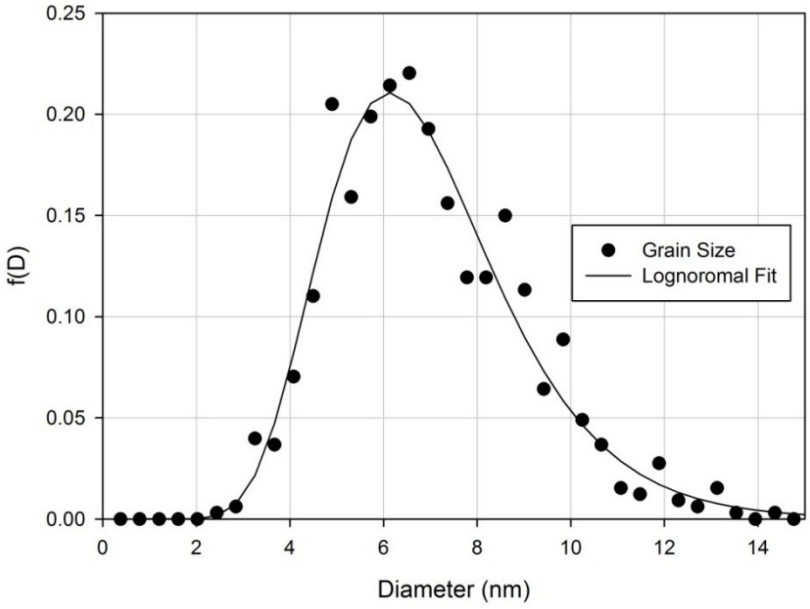

Figure 25: Example of the quality of fit achieved when n>500 grains are measured.

4.4. The York Protocols

In the study of exchange biased materials there are two major problems that are encountered when trying to characterise a sample in a reproducible manner. The first of the problems is due to difficulty in heating up samples with technological applications to the Néel temperature of the AF layer. For $IrMn_3$, the current material of choice, T_N is ~900K [34] which is sufficiently high to cause diffusion in multilayer films. However due to the granular structure of a polycrystalline material it is possible to set IrMn layers at temperatures as low as 475K. This is achieved through thermal activation of the AF lattice within each grain [22]. Furthermore thermal instability of the AF grains can lead to the state of order within the AF changing during a measurement leading to non-reproducible measurements of parameters such as H_{ex} and H_C. To overcome these issues a careful control over the thermal and magnetic history of the AF is necessary. This ensures a uniform state at the beginning of a measurement that can be reproduced [3].

The second problem is due to the fact that the AF does not provide a signal in conventional magnetic measurements it is necessary to observe changes in the AF via their effects on the F layer. This can only be done through careful control of the thermal and magnetic history of the AF. By using a specially designed set of magnetic field and temperature protocols, dubbed the York Protocols, it is possible to control the state of order in the AF reproducibly to a high resolution [3].

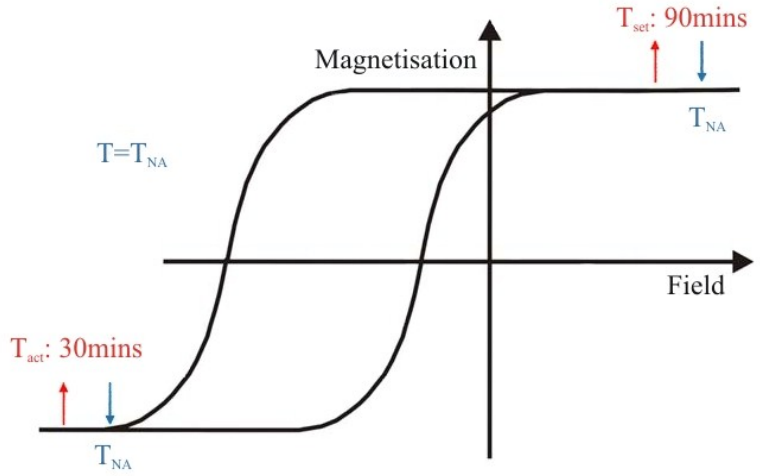

Figure 26: Schematic diagram of the York Protocol [3].

Post-deposition the state of the AF is both unknown and non-reproducible. As such the first step in the York protocol is to ensure that the AF is set in a reproducible manner. This is done by heating the sample to the maximum temperature which does not result in diffusion (T_{set}). Simultaneously a magnetic field that is sufficient to saturate the F layer is applied in the known direction of the easy axis. Due to the wide distribution of energy barriers in the AF the magnetisation follows an *ln t* law. This gives rise to a $\ln t_{set}$ law for the degree of order (*P)* in the AF which then controls H_{ex}. The setting process then has a time dependence coefficient $S\left(=(dp/d\ln t)\right)$ that is defined as

$$S = 2P_s k_B T f(\Delta E_C) \tag{30}$$

where P_s is the saturation value of the AF order and $f(\Delta E_C)$ is the critical value of the energy barrier at the setting temperature [57]. With a setting time of 90mins the change in H_{ex} is <1% allowing for reproducibility of H_{ex}.

Once the AF is set in a reproducible state it is necessary to find the temperature at which no thermal activation (T_{NA}) occurs for the sample during the time of measurement of the system. This is done by cooling the sample down to T_{NA} in the setting field. T_{NA} is ascertained by first cooling to a trial T_{NA} and then reversing the field so that the F layer saturates in the opposite orientation to that used for the setting. The sample is held in such a state for a short period and then a hysteresis loop measured. The process is then repeated however a reverse setting period of 30mins is chosen. If the resulting hysteresis loop is different to that of the initial one thermal activation has occurred and a lower T_{NA} is required. Once the sample is fully set and T_{NA} known it is possible to undertake controlled thermal activation [3]. This is shown schematically in figure 26.

4.4.1. Measurement of the Blocking Temperature

The blocking temperature T_B of a material is classically defined as the temperature at which H_{ex} goes to zero. Originally the method to determine T_B was to measure hysteresis loops with increasing temperatures until the loop shift became zero. This value of T_B corresponded to the AF grain with the largest anisotropy energy [22]. In polycrystalline thin films each AF grain has its own blocking temperature and the AF is therefore characterised by a distribution of blocking temperatures.

With the York protocol this distribution is measured through careful thermal activation of the AF layer. The method is similar to that for finding T_{NA}. After setting the sample for 90mins it is then field cooled to T_{NA} and a reverse field held for 30mins and a hysteresis loop measured. The process is then repeated however whilst applying the reverse field the sample is heated in progressively larger amounts. Heating whilst the F layer is reversed changes the order within the AF from the original state to the opposite orientation as shown in the figure 11. The amount of the AF that undergoes thermal activation is then a function of the temperature and exchange field from the F layer. The value of H_{ex} can then be seen as proportional to the difference in the fractions of the AF grains orientated in opposite directions [3].

$$H_{ex}(T_{act}) \propto \int_{T_B}^{\infty} f(T_B)\, dT_B - \int_{0}^{T_B} f(T_B) dT_B \tag{31}$$

Equation 31 relies on the coupling between the F and AF grains being independent of AF grain size. This definition leads to a different definition of T_B. In these measurements T_B occurs when equal fractions of the volume of the AF grains are orientated in opposition corresponding to the median blocking temperature $\langle T_B \rangle$. The conventional definition of T_B instead now describes the maximum blocking temperature of the distribution. All measurements obtained in this work were carried out using the York Protocol.

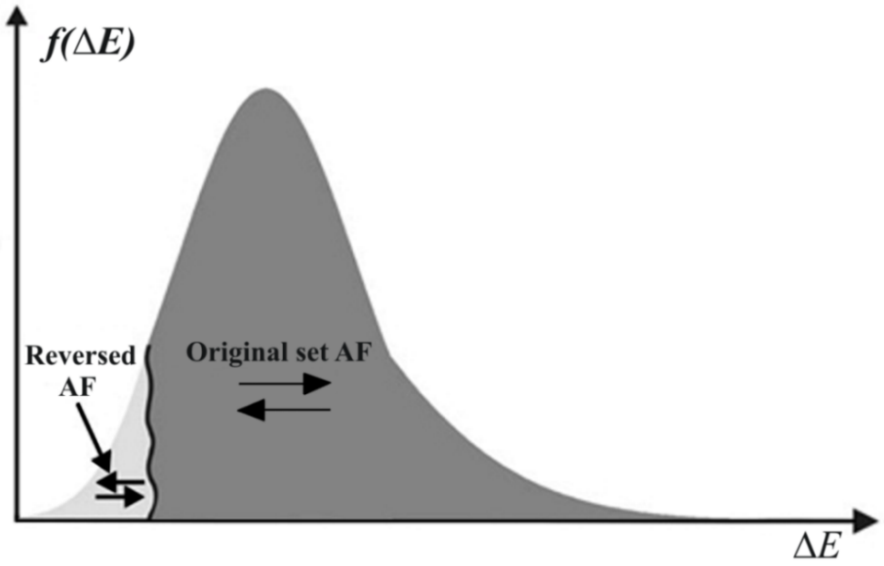

Figure 27: Schematic of the energy barriers to reversal [3].

4.4.2. Calculation of K_{AF}

As metallic polycrystalline AFs are an amalgam of grains distributed in size, typically 10nm, they are thought to contain a single AF domain. Single domain F and AF particles are subject to thermal activation and so lead to a magnetic transition over an energy barrier [21] [22]

$$\Delta E = KV_{AF} \tag{32}$$

where K is the anisotropy of the AF grain and V_{AF} its volume. This behaviour is observed below a critical volume which depends on measurement time and temperature. The relaxation time is given by the Néel-Arrhenius law [22].

$$\tau^{-1} = f_0 exp\left[-\frac{K_{AF}(1-H^*/H_K^*)^2}{k_B T}\right] \tag{33}$$

where f_0, the attempt frequency, is taken to be $10^9 s^{-1}$, k_B is Boltzmann's constant, V is the grain volume, T is the temperature and K_{AF} is the AF grain anisotropy [35]. H_K^* is the pseudo-anisotropy field similar to that of the anisotropy field in a F. H^* is the exchange field from the F layer acting on the AF layer which causes a decrease in ΔE of the AF grains. The limiting case of ΔE is taken to be $K_{AF}V$. Both H^* and H_K^* are unknown but H^*/H_K^* has been shown to be small for most systems used in applications [58]. Due to the magnetocrystalline origin of K_{AF} it is temperature dependent in the form

$$K_{AF}(T) = K_{AF}(0)(1 - T/T_N)^n \tag{34}$$

where n is unity based on $K_{AF} \propto [m_{AF}(T)/m_{AF}(0)]^3$ and the approximation $m_{AF}(T) \propto (T - T_N)^{1/3}$ where m_{AF} is the moment of one of the AF sub-lattices [59].

Through use of the York Protocol the issue of thermally disordered grains can be removed and allow the calculation of K_{AF} for the set fraction. At the point where $\langle T_B \rangle$ is calculated the interfacial coupling parameter C^* can be negated as [3]

$$H_{ex}(\langle T_B \rangle) \propto C^* \left[\int_0^{\langle T_B \rangle} f(T_B) dT_B - \int_{\langle T_B \rangle}^{\infty} f(T_B) dT_B \right] = 0 \tag{35}$$

allowing for the calculation of K_{AF} at that temperature. By assuming columnar growth of the grains the median grain volume can then be calculated using

$$V_m = \pi D_m^2 t_{AF}/4 \tag{36}$$

where t_{AF} is the thickness of the AF layer and D_m is the previously found median grain diameter. By substituting this into equation (10) K_{AF} at $\langle T_B \rangle$ can be calculated using

$$K_{AF}(\langle T_B \rangle) = \frac{\ln(t f_0)}{V_m} k_B \langle T_B \rangle \tag{37}$$

By equating equations (34) and (37) it then becomes possible to calculate K_{AF} at any required temperature.

4.4.3. Setting Field Dependence

It is known in the magnetic recording industry that a large field is required to set the AF layer in a spin valve and tunnel junction head. As the typical Fs used in the magnetic recording industry saturate in a few hundred Oe they are certainly saturated by the 20kOe and greater fields used. As it is generally understood that the exchange field from the F layer aligns the AF grains there should be no benefit to applying a field larger then saturation. This is clearly not the case as increases of H_{ex} to the scale of 10 and 20% can be seen with a setting field of 20kOe. As such it is thought that the changes are due to changes in the interface spin order as described in section 3.2.2 [3].

Using the York Protocol it is possible to measure the effect of setting field on H_{ex}. Following the protocol and setting the sample at a field, say 5kOe, and then measuring at T_{NA} and repeating with progressively higher fields it is possible to observe the effect on the interface of an enhancement of the system.

Chapter 5. Results

5.1. Interfacial Doping of Exchange Biased Thin Films

As has been shown exchange biased thin films experience a wide range of current and future applications. As such a good control over the properties of thin films is required to suit a variety of tasks. One of the avenues for achieving this is the modification and control of the interface between the F and AF layers. This study is concerned with the insertion of atomic layers of specific elements, in particular Mn, at the interface of CoFe/IrMn sputtered polycrystalline thin films.

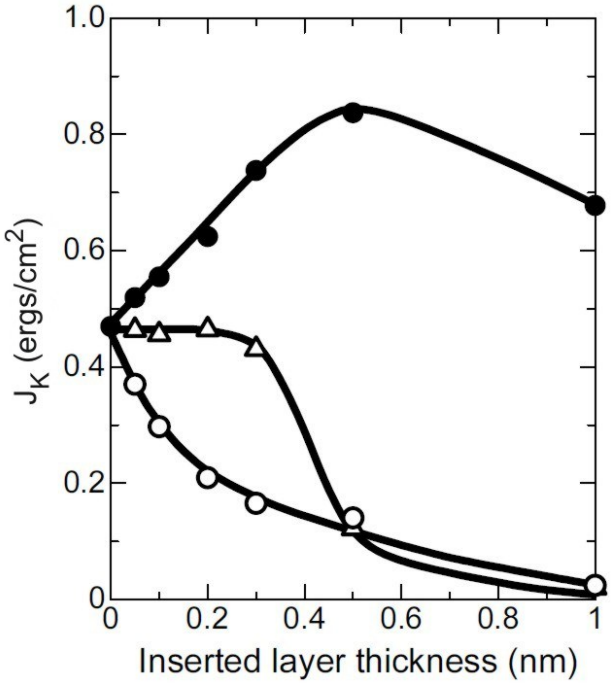

Figure 28: Graph showing the results of Tsunoda et al. [44] where the unidirectional anisotropy constant, J_K, is varying with respect to inserted layer thickness in $Ir_{25}Mn_{75}$(10nm)/X/$Co_{70}Fe_{30}$(4nm) bi-layers. The inserted layers X = Mn (closed circle), Tb (triangle) and Pd (circle).

The effects of different layer materials and the effect of their thicknesses can be observed in figures 28 and 29. Tsunoda's [44] results showed a decrease in the exchange anisotropy for increasing thicknesses of Ru, Ta, Pd, Gd and Tb interfacial layers whilst an increase of nearly 50% was observed in the case of Mn. The results in the case of Tb, Pd and Mn are displayed in figure 28. Tsuonda et al. explained that the decrease is due to the blocking of the exchange interaction. In the case of the Mn Tsunoda proposed that the modification of exchange bias was

not due to a change in crystalline structure but the magnetic structure. Specifically it was proposed that the increase was due to a modification of the spin structure of the AF at the interface.

Ali et al. [60] explored the effects of doping through insertion of a number of different elements of varying thickness at the interface. It is important to note that as the F layer used was Co an increase in the loop shift (H_{ex}) is observed in the case of Fe, Ni and NiFe. This fits with diffusion of the materials into the F layer creating alloys at the interface, such as CoFe, which provides a greater exchange bias. Also the lattice matching between Co, a material that experiences close packing fcc and hcp structures, with that of IrMn, an fcc structure, is rather poor. Introduction of elements at the interface at thicknesses under an atomic layer could improve the lattice matching increasing H_{ex}. Pt was also shown to increase H_{ex} for thicknesses of around 1 – 2 atomic layers. A similar explanation for this increase can be assumed in that Pt spacers are known to improve the alignment of Co spins out of plane increasing H_{ex}. Ali et al. state that this could be due to formation of PtMn at the interface which has a higher anisotropy than IrMn. It is worth noting that in neither work were the samples confirmed to be at T_{NA} and therefore the results are not reproducible. As such a reliable explanation of the results is not possible without further analysis.

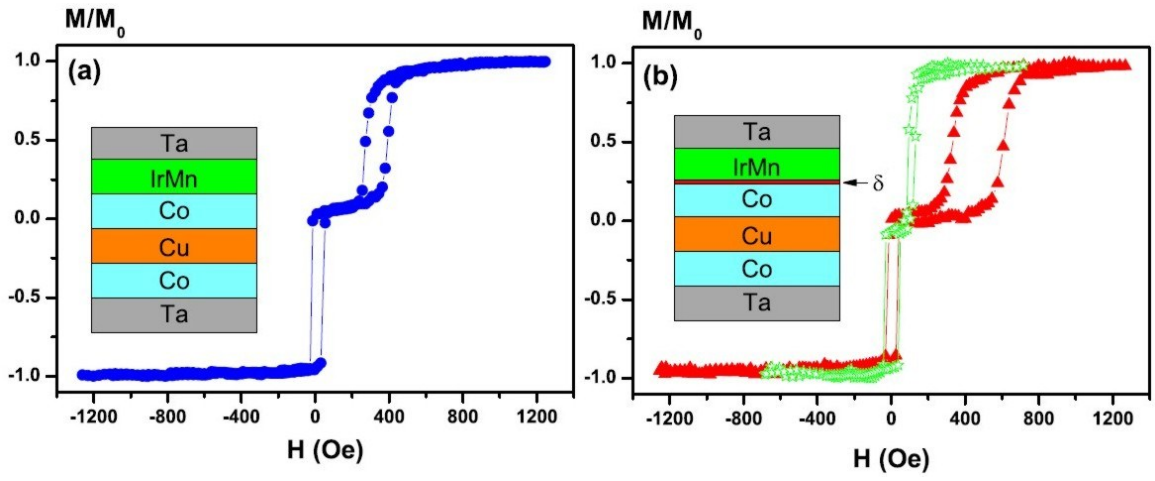

Figure 29. Graph showing the variation in loop shift H_{ex} when a Co(2.6nm)/IrMn(12nm) bilayer (blue circles) is doped at the interface with 0.1nm of Fe (red triangles) and Ta (green stars) [60].

The results of Tsunoda were confirmed using a sample structure of Si(100)/Ta(5nm)/Ru(5nm)/IrMn(10nm)/*X*/CoFe(2.5nm)/Ta(5nm). In the structure X represents approximately one atomic layer of Mn, Co, Cu, Ta or Fe. The results of this experiment are shown in figure 30. As can be clearly seen H_{ex} decreased by 35-100% in all cases apart from Mn where an increase of 26% was observed. It was hypothesised that the enhancement of H_{ex} due to the insertion of Mn is caused by intermixing at the interface. It has been found [61] that Mn easily diffuses into CoFe and vice versa. This creates a Mn deficiency at the interface decreasing H_{ex}. Through the addition of a monoatomic layer at the interface this Mn deficiency is reduced and an increase in H_{ex} observed. Aley et al. [40] did a number of experiments in which the composition of the IrMn was varied. A 'top hat' relationship of H_{ex} with respect to Mn concentration was found. Simultaneously a linear increase in K_{AF} with increasing Mn was also shown, both of which are shown in figure 19. As such if the increase in H_{ex} is a variation in IrMn composition a similar behaviour would be expected.

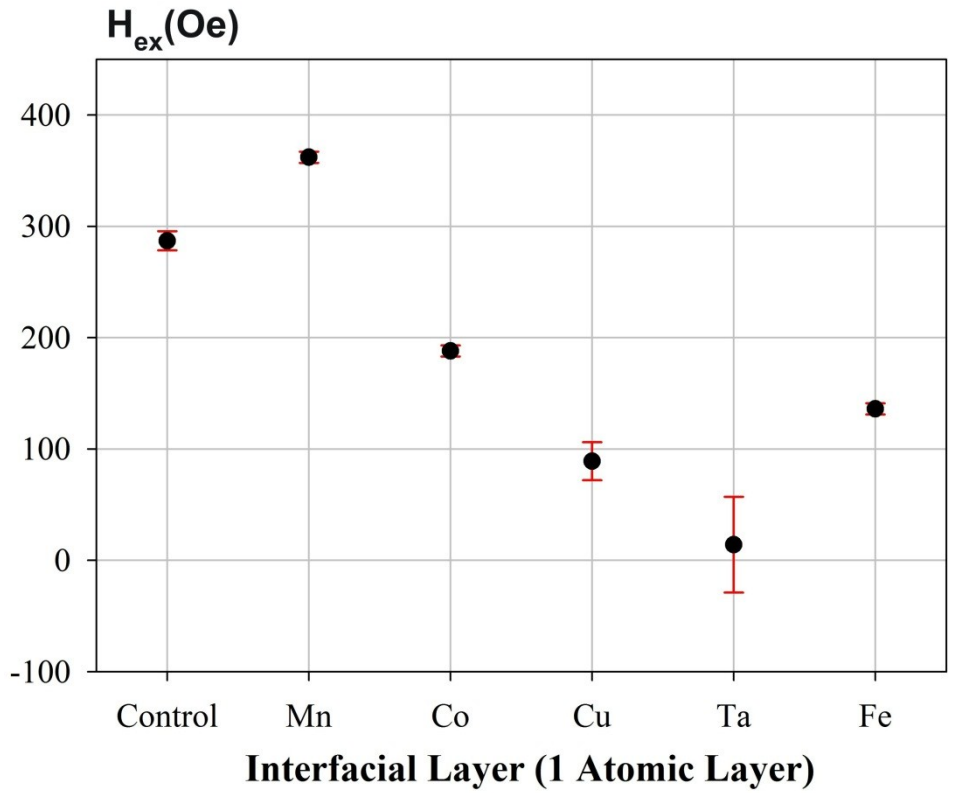

Figure 30: Comparison of the change in H_{ex} due to the insertion of approximately 1 atomic layer of Mn, Co, Cu, Ta and Fe at the F/AF interface

The aim of this study is to find the origin of the modification to H_{ex} due atomic Mn layers at the interface of CoFe/IrMn bi-layers as reported in literature [60] [44]. This was carried out by producing a set of six samples of composition Si(100)/Ta(5nm)/Ru(5nm)/IrMn(10nm)/Mn(*x*nm)/CoFe(2nm)/Ta(5nm) where *x* is 0, 0.3, 0.6, 0.9, 1.2 and 1.5 as shown schematically in figure 31. The samples were measured following the York Protocols in order to observe the effect of the Mn interfacial layer on the interface and the bulk properties of the system.

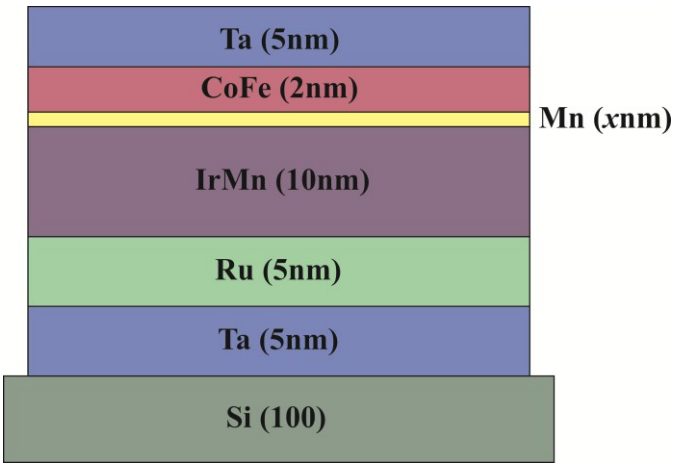

Figure 31: Schematic of the sample structure used in this study where *x* is the interlayer thickness of 0, 0.3, 0.6, 0.9, 1.2 and 1.5nm.

The sample structure was specifically chosen for its T_{NA} of 50°C and H_{ex} of >750Oe. It is known that the seed layer is vital for exchange bias. A strong (111) texture has been shown to create a large exchange bias and high $\langle T_b \rangle$ [62] [39]. A study by Aley et al. [39] compared the effects of Cu, Ru and NiCr seed layers. It was found that NiCr promotes a strong (111) texture, a result of which are anisotropies in the order of (3.3±0.4)x10^7 ergs/cc. This results in samples that, although stable at room temperature, cannot be set at temperatures below 250°C. In contrast a Cu seed produced a poor (111) texture but could be set at lower temperatures. However these samples had an anisotropy of (0.28±0.02)x10^6 ergs/cc and were not thermally stable at room temperature. Therefore a Ru seed layer was chosen. This is because the samples produced are thermally stable at room temperature and can be fully set at temperatures under 250°C using fields under 20kOe [39].

A layer of fast sputtered Ta was grown initially as it is amorphous and promotes perpendicular to plane hcp growth of the Ru layer [63]. The thickness of the IrMn

layer was chosen to be 10nm because it has been shown that the T_{NA} is room temperature or just below for such samples [3]. It is also well established that the F layer thickness is proportional to H_{ex} [35]. It has been shown that CoFe thicknesses of >3nm have a T_{NA} at room temperature [35]. As such a CoFe layer of thickness 2nm was chosen to achieve as large a value of H_{ex} as possible whilst achieving the desired T_{NA}. A capping layer of Ta was deposited in order to reduce oxidisation and protect the samples from physical damage.

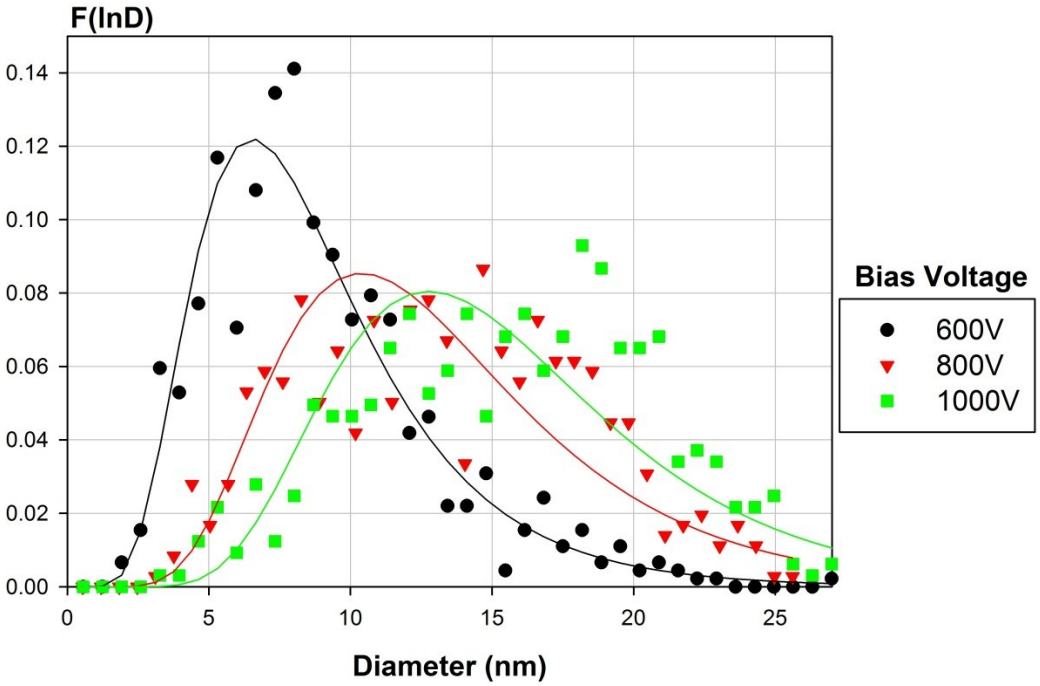

Figure 32: The log-normal distributions, *F(lnD)*, for Ru(5nm)/IrMn(10nm)/Mn(0.3nm)/CoFe(2nm) bi-layers when grown at different bias voltages.

The samples were produced in a HiTUS system, as described in section 4.1.1, using an RF power of 1.5kW and Ar operating pressure of 2.7×10^{-3} mbar. These two parameters were chosen based on the studies of Vopsaroiu et al. [51]. In their study it was demonstrated that grain size was controlled through deposition rate. Accurate control over the Mn layer thickness was required as well as thermal stability at room temperature. As faster deposition rates resulted in larger, and therefore more thermally stable grains a compromise between large grains and slow deposition needed to be found.

A preliminary experiment using Ru(5nm)/IrMn(10nm)/Mn(0.3nm)/CoFe(2nm) bi-layers was carried out in order to find the ideal bias voltage. Figure 32 shows the

variation in grain size distribution for different bias voltages that were fitted using a log normal distribution as described in chapter 4.3.2. For the chosen bias voltages the median grain diameter varies from ~7 to 13nm with the distribution widening with increasing size. A narrower distribution would be preferred as it would provide a narrower, and therefore easier to compare, T_b distribution. However the grain sizes of the sample grown at a bias voltage of 600V fall beneath the V_C limit for a Ru seed. As such they possess a T_{NA} beneath room temperature. Although a lower T_{NA} would resolve this issue it would require the use of cooling. As the 800V and 1000V samples have a T_{NA} of around 40°C the level of complexity added to the experimental procedure would not be worth the gains. As such the T_b distributions for the 800 and 1000V cases were found and are shown in figure 33. It was found that utilising 800V or 1000V bias voltages resulted in an increase in H_{ex} of 13% and a decrease in $\langle T_b \rangle$ of 15-20°C was observed. As such the 800V bias voltage was chosen because with a slower deposition rate more careful control over layer thickness is possible.

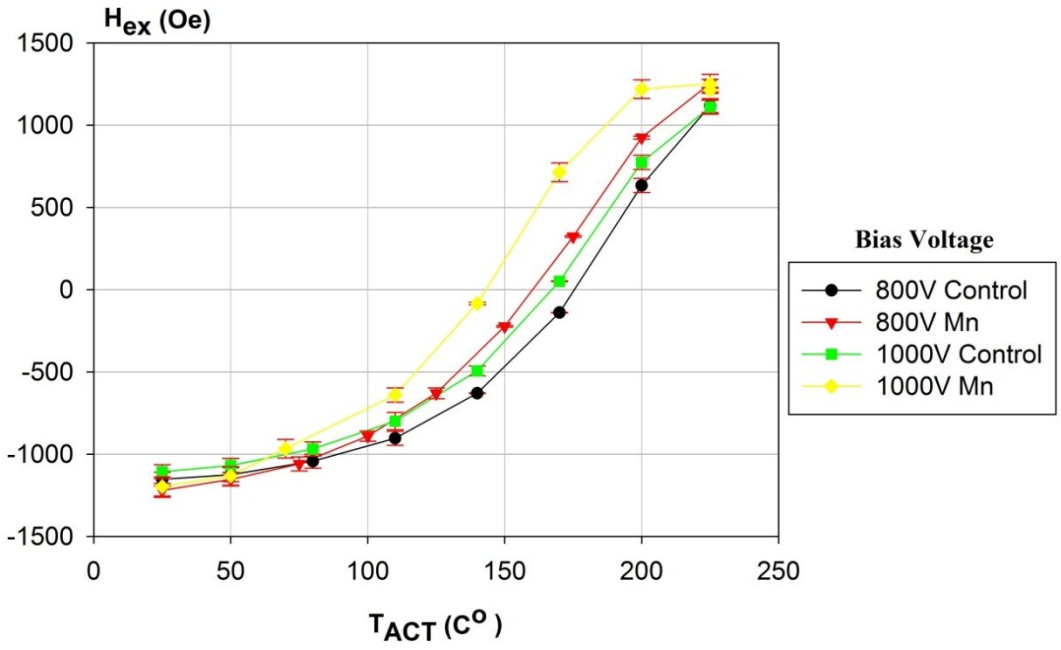

Figure 33: Comparison of the variation in H_{ex} when reversed with different activation temperatures T_{ACT} with the addition of Mn at the interface of CoFe/IrMn bi-layers sputtered at bias voltages of 800 and 1000V.

5.1.1. Variation in H_{EX} due to Interfacial Mn Layer

All measurements in this study were carried out using a MicroSense Model 10 VSM, as described in section 4.2.2, which was equipped with a constant-flow air cryostat of temperature accuracy of 0.1K over one hour. Before any measurements were taken the samples were annealed at a temperature of 225°C under a 5kOe applied field as per the York Protocols. A 5kOe setting field was used as this is more than sufficient to set CoFe which has a value of H_{sat} of <500Oe. After setting, the samples were field cycled in order to remove the athermal training effect [37] [4] from subsequent measurements to ensure reproducibility, as described in section 3.2.2.

The results of the measurements can be seen in figure 34. A quite clear increase in H_{ex} is found with the addition of up to two mono-layers of Mn; however any subsequent increase in thickness causes a decrease. These confirm the results observed by Tsunoda et al. [44] albeit a smaller enhancement of only 12% is observed which peaks at 0.3nm, whereas Tsunoda found the peak to occur at around 0.6nm. The disparity in results could quite easily have arisen due to variations in sample production as Tsunoda utilises a magnetron sputtering system in a UHV environment. Similarly variations in target compositions could be responsible especially as it is known that Mn sputters at a higher rate than Ir. This could lead to a slightly different stoichiometry to that present in the target. A further difference arises as the results shown in figure 34 were measured at T_{NA} whilst the state of the samples in Tsunoda's results is unknown. This makes an accurate comparison difficult.

Table 1 shows the values of both H_{ex} and H_C obtained from this measurement. As can be seen there is a clear increase in both H_{ex} and H_C with the addition of 0.3 and 0.6nm of Mn. What is quite interesting is that the peak in both values seems to occur at different points, with H_{ex} at 0.3nm and H_C at 0.6nm. Taking these results into account a hypothesis can be formed before entering into the main body of the results. It has been shown that Mn at the interface diffuses readily into the CoFe layer creating a Mn deficient interface [40]. If this were the case then a variation in the interfacial properties of the system and not the bulk would be expected.

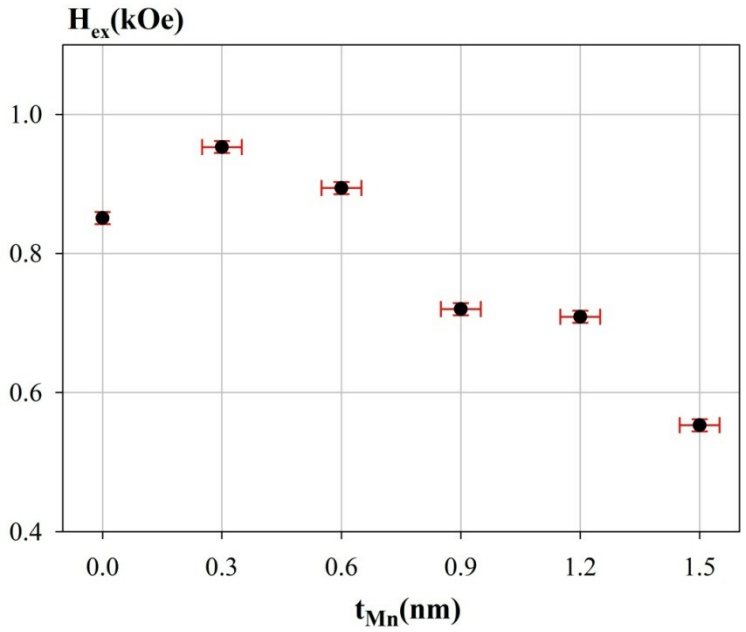

Figure 34: Variation in loop shift H_{ex} which the addition of 0-5 atomic layers of Mn.

The preliminary results in figure 33 raise this hypothesis to question as there is a clear decrease in $\langle T_B \rangle$ for both samples. In the case of the 1000V sample a decrease is observed in the order of 35-40°C. This implies that there is some variation in the bulk of the system, however according to the work of Aley et al. [40] an increase in $\langle T_B \rangle$ would be expected. Even more interesting is that the change in $\langle T_B \rangle$ is larger by about 10°C between the 800V and 1000V cases whilst they have the same increase in H_{ex} due to the Mn interfacial layer. The origin of this could potentially be due to the inherent variations in sample growth. Further results are required, of course, before a full analysis can be carried out.

Mn Thickness (nm)	H_{ex} (±10 Oe)	H_C (±10 Oe)
0	851	200
0.3	953	215
0.6	884	230
0.9	720	155
1.2	709	145
1.5	559	95

Table 1: Key magnetic measurements results after initial setting at 5kOe with athermal training removed.

5.1.2. Grain Size Distribution

TEM images were obtained of the samples using a JEOL 2011 TEM. As described in section 4.1.1 carbon coated copper grids were simultaneously sputtered and it is from these that TEM images were obtained. The grain size distribution was measured using an equivalent area method and fitted with a log normal distribution as described in section 4.3.2 and median grain volume V_m calculated based on the columnar growth of the grains. As this is the AF grain size distribution the length of the column is taken to be the thickness of the AF layer.

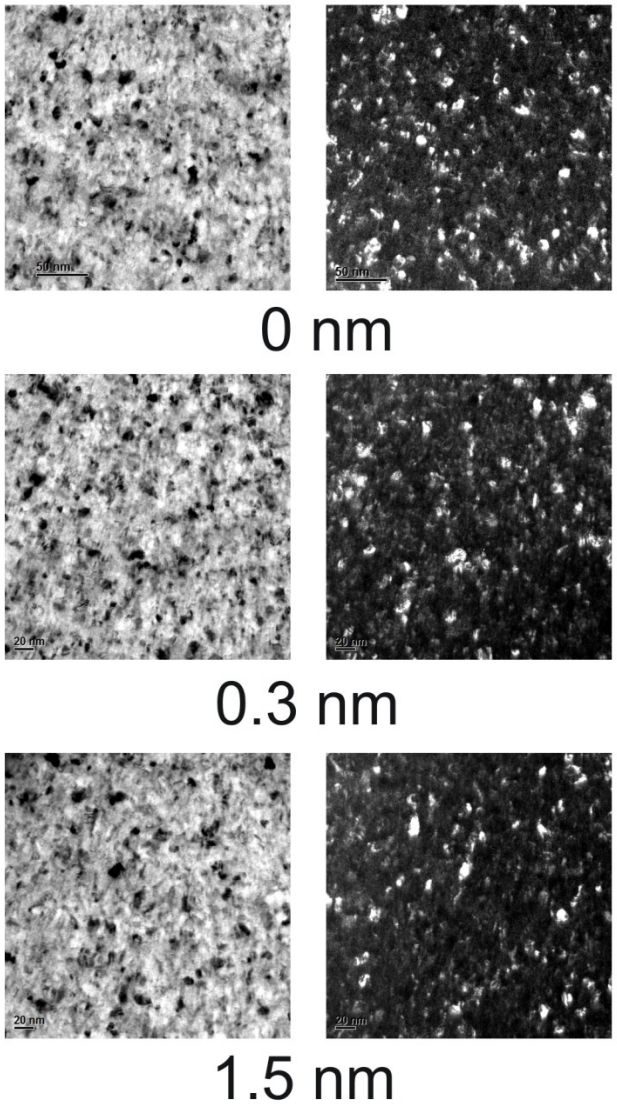

Figure 35: Three standard images obtained for the cases of 0, 0.3 and 1.5nm Mn interfacial layers taken simultaneously in bright and dark field modes.

The results as shown in figures 35 and 36 were taken at a magnification of 60,000x in order to achieve a minimum of 30 measureable grains per image. Thirty images per sample were taken so as to obtain 900+ grains. An image in the dark field was taken simultaneously for comparison during grains size analysis due to the Bragg condition as explained in chapter 4.3.1. This method was developed based on advice from Prof. J. N. Chapman of Glasgow University and involves the comparison of the dark field image to the bright field image. This enables easier identification of grains that fit the Bragg conditions. This was done to ensure a very good log-normal distribution for direct comparison. Examples of the images are shown in figure 35. As can be seen qualitatively there is no obvious difference between the three samples.

Through measuring the grain size distribution and fitting a log-normal curve a quantitative comparison can be carried out. As can be seen in figure 36 and table 2 the addition of 0.3nm of Mn at the interface had little effect on the grain volume distribution. As can be seen there is little variation in the median diameter or volume with relatively similar standard deviations. With the addition of 1.5nm of Mn at the interface an increase in V_m of ~150nm^3 is observed however the standard deviation remains the same. The increase in the median diameter in the case of a 1.5nnm Mn interfacial layer could correspond to an equivalent increase in the AF layer thickness. Compared to the similar results shown in figure 13 [3] the difference in grain volume between a 10nm and 12nm thick AF layer are not too dissimilar to that seen in figures 36.

In order to calculate the grain volumes of all the samples a magnification of 80,000x was used. This was done to ensure that again at least 30 grains could be counted per image; however the higher magnification allowed for less ambiguity about the variation in size. A lower resolution in the distribution was required and so the minimum number of grains required for a good log normal fit, 500, were measured.

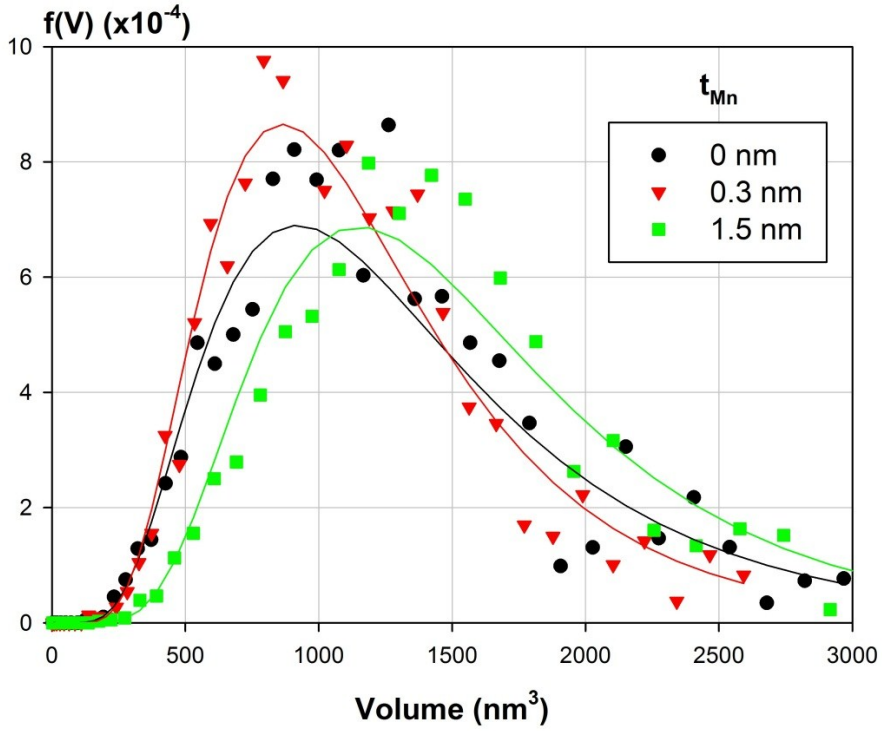

Figure 36: Graph comparing the grain volume distributions for samples with 0, 0.3 and 1.5nm Mn interfacial layer.

The results as shown in figure 37 and table 2 indicate that the thickness of the Mn interfacial layer has no effect on V_m within error up to the addition of 1.5nm of Mn. This result agrees with the shift in the distribution as observed in figure 36.The grain volume is calculated using equation (38).

$$V = \frac{\pi D^2 t}{4} \tag{38}$$

The two sources of error in the grain volume are therefore dependent on D and the layer thickness, t. When ≥500 grains are measured the error in D_m is around 0.1-0.2nm. The error in t dominates the error at 10% as found by Dr N. P. Aley. This however is solely the measurement error and not sample error. As can be seen through the trend line drawn in figure 37 both the 0.3 and 1.5nm points are not on the line. This small variation is most likely an example of the error associated with sample production as opposed to measurement. It is important to note that the thickness of the AF layer was assumed to be a constant 10nm even with the addition of >1nm of addition material at the interface. This assumption was made as bulk Mn is not an AF and only a small portion of the thicker Mn layers could be considered physically 'part' of the AF layer.

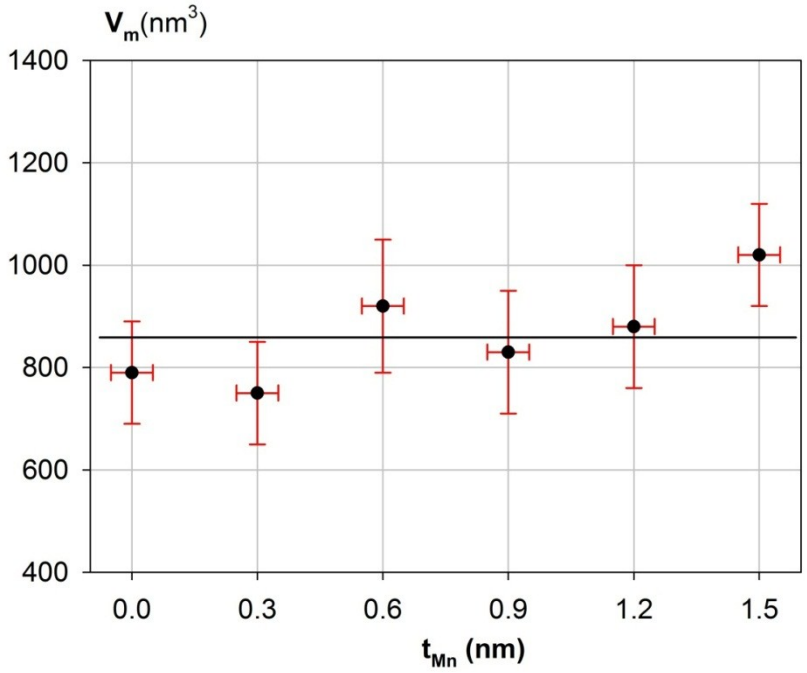

Figure 37: The variation in median grain volume V_m with the addition of 0-5 atomic layers of Mn.

It is expected that a layer deposited at the interface of the F/AF should have little or no effect on the grain size. This is because the grain size should be established through both the seed layer and AF layer. A possible explanation for this is that once the Mn layer thickness approaches a thickness of greater than a few atomic layers it will begin to have the effect of increasing the AF layer thickness. Similar results as seen in figure13 [3] show that the difference in grain volume between a 10nm and 12nm thick AF layer can be in the scale observed here. However this should lead to a matching change in $\langle T_B \rangle$.

Mn Thickness (nm)	d_M (± 0.5 nm)	σ_{lnD}	V_m (±10% nm^3)	σ_{lnV}
0	10.0	0.27	870	0.36
0.3	9.9	0.24	720	0.36
0.6	10.8	0.25	920	0.35
0.9	10.3	0.27	830	0.35
1.2	10.6	0.24	880	0.35
1.5	11.4	0.24	1030	0.35

Table 2: Grain size distribution results

5.1.3. Blocking Temperature Distribution

The blocking temperature distribution for each sample was measured following the York Protocols as described in section 4.4.1. Seven data points were measured as this was deemed sufficient to get a reasonable distribution without taking an unreasonable amount of time. Prior to the main body of results a trial run was carried out, as shown in figure 33, on a set of test samples in order to predict the size of the change in H_{ex}. This allowed for greater accuracy without sacrificing time. The samples were set and activated at temperatures of 250°C in order to achieve full alignment. As can be seen in figure 38 this was successful as there is no variation in H_{ex} between 210 and 250°C.

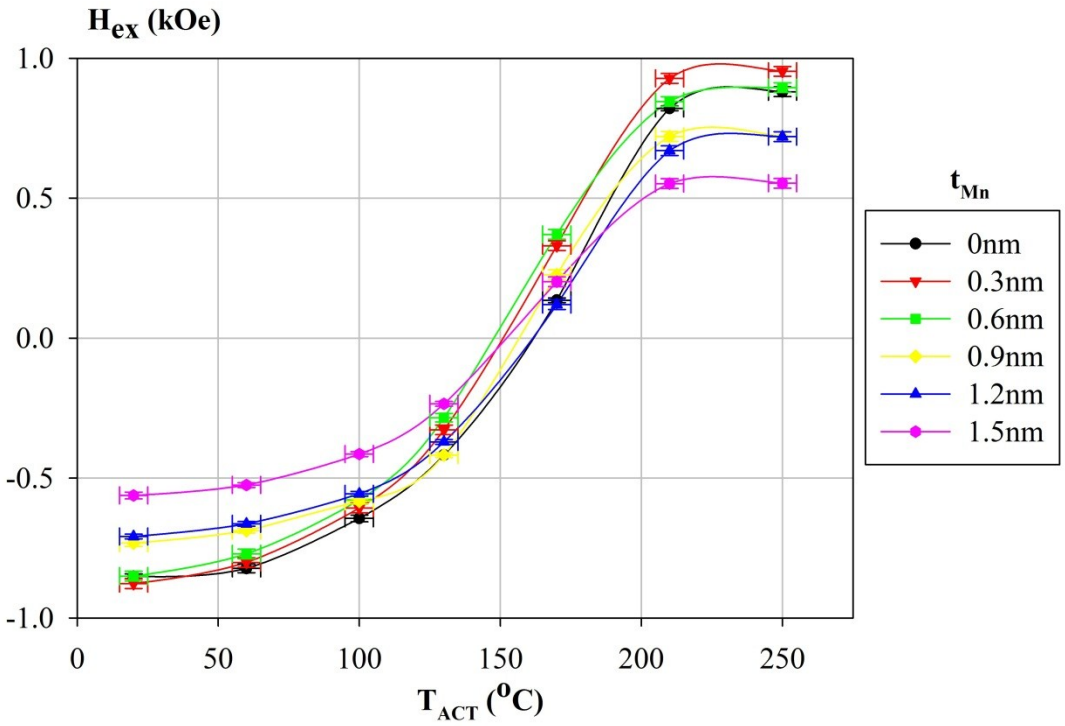

Figure 38: Results showing the variation in the blocking temperature distributions for different Mn interfacial layer thicknesses

Figure 38 matches, in the case of the 0.3nm sample, the preliminary results as seen in figure 33. However when seen in conjunction with the results for samples with 0.6-1.5nm of Mn it is clear that there is no significant change in the median blocking temperature with the addition of Mn. This is further confirmed by the near identical spread in the values of T_B with all the samples being thermally stable up to 50°C and fully set by 225°C. This result confirms the relative lack of change in

the shape of the grain size distribution as show in figure 36. According to equation (23) reproduced below it is possible to ascertain whether a variation to the system affects the bulk or interfacial properties of the system. If a change in the value of $\langle T_B \rangle$ with respect to the Mn interfacial layer thickness is observed then a variation in the bulk properties will have occurred. This is because, as shown in equation 23, when reversed at $\langle T_B \rangle$ the volume integral is equal to zero and so is independent of C^*.

$$H_{ex}(T_{meas}) = H_{ex}^{i} C^{*}(H_{set}, T_{set}) \int_{V_C}^{V_{set}} V f(V)\, dV$$

As can be seen in table 3 $\langle T_B \rangle$ does not change within error due to the insertion of mono-atomic layers of Mn at the interface. This result agrees with lack of variation of grain volume as shown in table 2 and figure 37. The shape of the T_B distributions similarly does not vary as is confirmed by the spread of the distributions as shown in table 2 and figure 36. This lack of change contradicts the results as found in the preliminary work shown in figure 33. It is highly likely that this discrepancy is due to variations in the sample growth. The 1000V sample was grown last out of the series of samples and throughout a growth session the operating temperature will generally increase from ~30°C to up to 100°C. This problem was reduced in the final results as the set of six samples were grown over two days, as opposed to just one. This was further confirmed as these samples were preceded by an identical set plagued with the same issues as the preliminary results. In these samples the same overall results were obtained with, however, larger errors.

Mn Thickness (nm)	$<T_B>$ (±5 K)
0	433
0.3	423
0.6	420
0.9	429
1.2	433
1.5	425

Table 3: Median blocking temperatures

The thermal activation results shown in figure 38 raise a question as to the increase in median grain volume observed in the case of the 1.5nm insertion layer. It is possible that although the median grain volume has increased the blocking temperature has not, as a change in the magnetic structure is solely occurring at the interface. This would give a small change in the median grain volume with no observable change in $\langle T_B \rangle$. This justifies the usage of a constant AF layer thickness. This is because in a 10nm thick film adding 1nm of material is increasing the thickness by 10%. This should lead to a change in $\langle T_B \rangle$ of 40K which is clearly not the case.

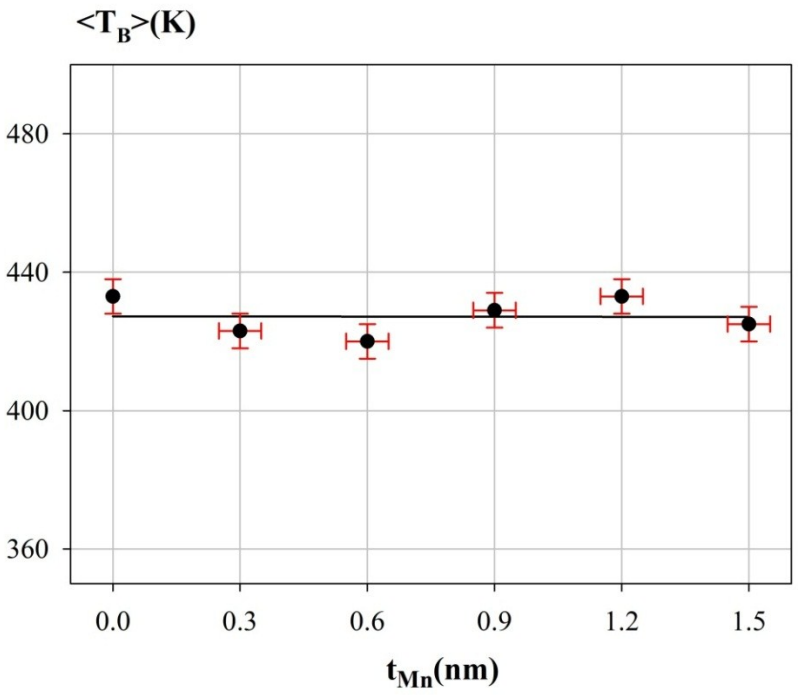

Figure 39: Results showing the variation in the measured median blocking temperature $\langle T_B \rangle$ with respect to a variation in Mn interfacial layer thickness.

5.1.4. AF Anisotropy

In order to calculate $K_{AF}(\langle T_B \rangle)$ for each sample the following values were used: t = 1800s, f_0 = 1x10^{9}s^{-1}, T = $\langle T_B \rangle$, T_N = 690K. The value of t was chosen as this was the setting time for the samples. The value of n was chosen to be unity as explained in chapter 4.4.2. The errors were calculated based on the experimental errors obtained through statistical analysis of the grain size and $\langle T_B \rangle$.

$$K_{AF}(\langle T_B \rangle) = \frac{\ln(t f_0)}{V_m} k_B \langle T_B \rangle \tag{38}$$

As can be seen in figure 38 and table 4 there is no variation in K_{AF} within error. This is clearly seen as the value of K_{AF} is proportional to $\langle T_B \rangle$ and inversely proportional to V_m as shown by equation (38). Comparing this to the results in figure 37 and 39 the drop in K_{AF} corresponds to the compounding of the variations in the two results. As discussed in the previous section a source of additional error unrelated to the measurements errors is that of the sample growth. This sample reproducibility, although limited in its affect, is still enough to cause variations such as those observed in figure.

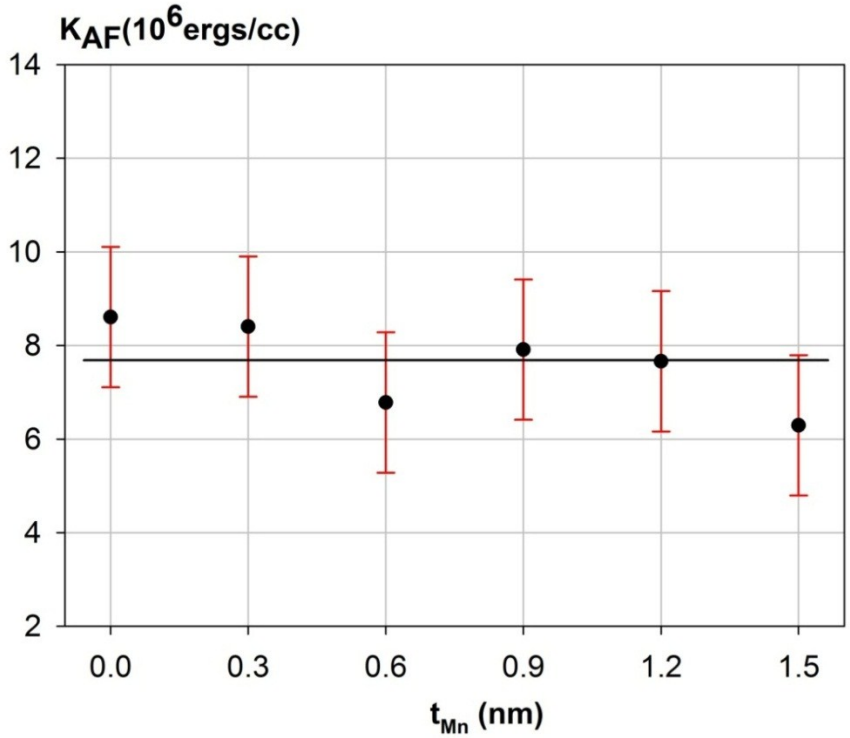

Figure 40: Results showing the variation in the AF anisotropy K_{AF} with respect to Mn interfacial layer thickness.

Comparing with the results of Aley et al. [40] an increase of K_{AF} in the order of $2x10^6$ergs/cc would have been observed if the origin of the variation in H_{ex} was due to an increase of Mn in the composition of the bulk of the AF grains. Considering the size of the increase in H_{ex} and the clear lack of systematic change in K_{AF} the change in the system is therefore most likely due to changes at the F/AF interface.

Mn Thickness (nm)	K_{AF} (10^6ergs/cc)	$<T_B>$ (±5 K)	V_m (±10% nm^3)
0	(9 ± 1)	433	870
0.3	(8 ± 2)	423	720
0.6	(7 ± 1)	420	920
0.9	(8 ± 1)	429	830
1.2	(8 ± 1)	433	880
1.5	(6 ± 2)	425	1030

Table 4: Graph showing the calculated values of K_{AF} alongside the two key values in its calculation.

5.1.5. Effect of the Setting Field

The effect of the setting field on the value of H_{ex} was measured for each sample as described in section 4.4.3. This was carried out by progressively setting each sample for 1 hour in field steps of 2.5kOe from 5kOe up to a maximum of 20kOe. The upper field limit was used due to field limitations of the ADE Model 10 VSM. The lower field limit was decided to be 5kOe as this was the field used to set the samples during the blocking temperature measurements. As the field required to saturate CoFe is <500Oe these fields are more than sufficient to saturate the F layer meaning any enhancement to H_{ex} is due to the effect on some portion of the AF. The bulk of the AF is not susceptible to the applied field apart from minor canting effects that may occur. Hence the effects must be due to uncompensated moments at the F/AF interface. As discussed in detail by Fernandez-Outon et al. [36] the type of effects observed are consistent with the spins existing in clusters with moments in the range of 10-50 μ_B.

The setting temperature used was 250°C based on the results for the blocking temperature distribution. The samples were field cycled to eliminate the athermal training effect. A hysteresis loop was measured during the field cycling in an attempt to observe the athermal training.

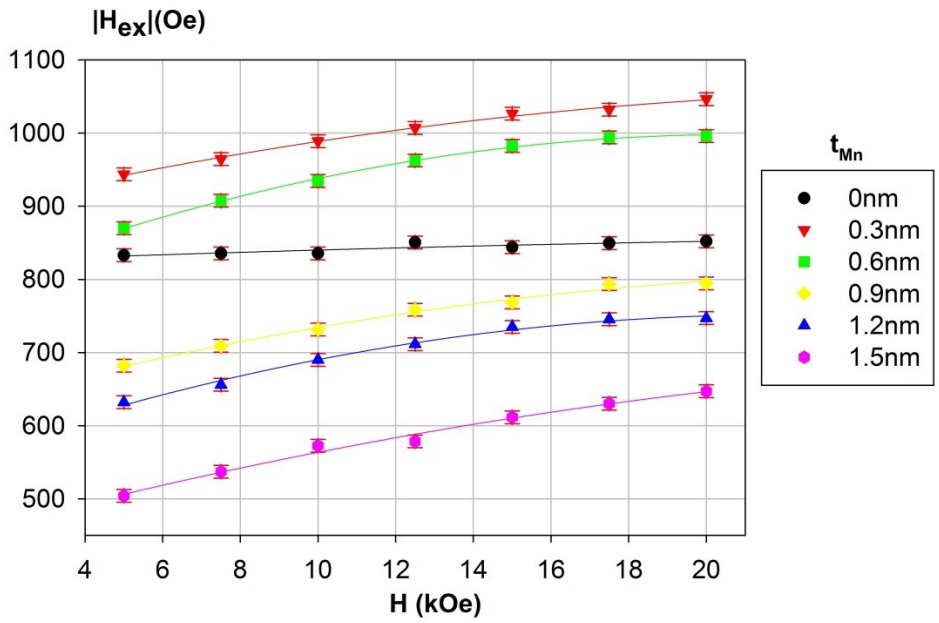

Figure 41: Results showing the effect of setting field H_{set} on exchange bias for different thicknesses of Mn at the interface

As previously discussed and shown again in figures 41 and 43 0.3 and 0.6nm of Mn at the interface increases the value of H_{ex} by ~100Oe and 50Oe respectively. Further layers of Mn serve only to decrease H_{ex} by up to 50%. Of interest though is the clearly large increase of 100-150Oe in H_{ex} due to a setting field of 20kOe with any addition of Mn. The contrast of these increases with the linearity of the H_{set} results in the 0nm case is striking. This change in the 0nm case is not unexpected however due to measurements currently being carried out in York. It has been initially found that between setting fields of 0 and 3kOe a large increase in H_{ex} is observed [64]. As H_{set} approaches 5kOe the increase flattens out to a gradient similar to that observed in the 0nm case. The shape of these curves is similar to that to a Langevin function of the form

$$\frac{M}{M_S} = \frac{N_S \mu_B (H_{eff} + H_{set})}{3kT} \tag{39}$$

where N_s is the number of spins within a cluster each with a magnetisation of a Bohr magneton (μ_B). The variable H_{eff} is the effective exchange due to the F-cluster, cluster-cluster, AF-cluster and spin-spin exchange interactions. In the work being done at York it has been found that by increasing grain size a behaviour that would be expected of an increase in N_s is observed. This model is conceptually shown in figure 18 which has been reproduced below.

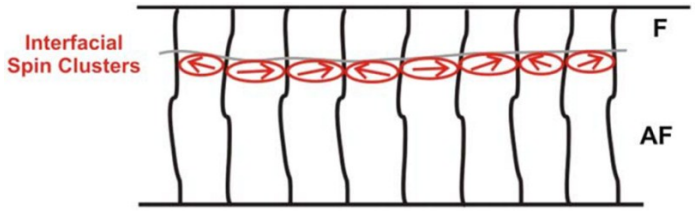

Figure 42: Schematic diagram of the interfacial spin clusters.

It is thought that the uncompensated spins at the F/AF interface within a grain behave not as individual spins but as a cluster. These clusters then order paramagnetically following a Langevin function as discussed in equation (39). As explained above with equation (39) these clusters feel a number of exchange interactions giving very complex behaviour. Returning to the results in figure 41 this paramagnetic ordering is observed. However with the addition of thicker layers of Mn the setting field ceases to be sufficient to saturate the clusters. An attempt to explain this increase in gradient/curvature with increasing Mn thickness will be carried.

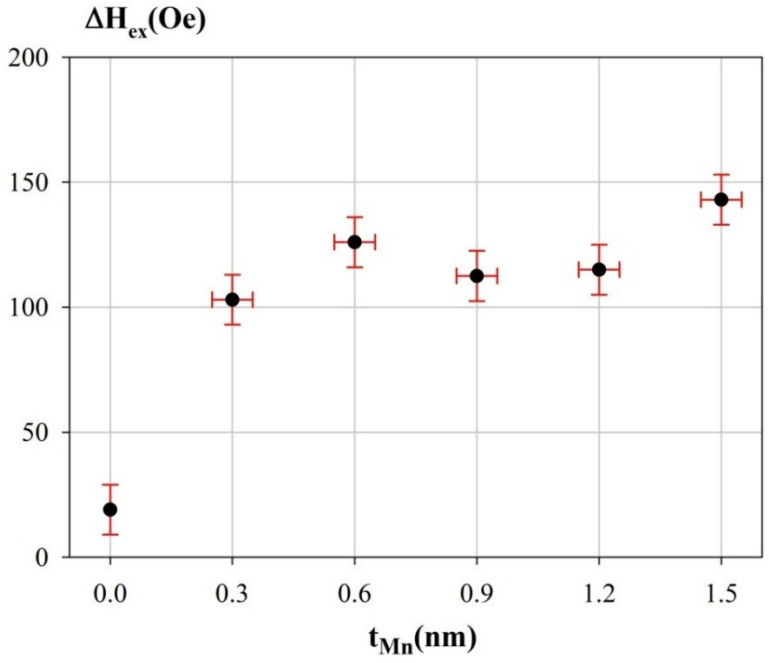

Figure 43: Graph showing the change in H_{ex} between 5kOe and 20kOe setting fields with respect to Mn interfacial thickness.

Figure 43 shows the change in H_{ex} between a 5kOe and 20kOe setting field. One could argue a steady increase in ΔH_{ex} with increasing t_{Mn} however, as previously discussed; this variation is probably due to sample production variation as opposed to an actual systematic increase. Therefore with the addition of Mn a

constant ΔH_{ex} of ~125Oe is assumed. This constant ΔH_{ex} matched with a variation in curve shape as shown in figure 41 as well as the increase and decrease in H_{ex} with Mn thickness implies a number of possible variations to the system.

Looking at equation (39) the easiest explanation for the shape of the curves in figure 41 is that with the addition of Mn at the interface N_s increases. As discussed by Tsunoda et al. [42] it is thought that it is the Mn spins at the interface that are responsible for the coupling leading to exchange bias. As such with the addition of Mn the volume and therefore number of spins present in the cluster will increase. However this does not explain the decrease observed in H_{ex} with Mn layers of thickness >0.6nm. This could be due to the spin clusters themselves not being aligned in the setting process as shown in the schematic in figure 18 that was reproduced above. This interpretation ignores not only H_{eff} but also the interdependence between H_{eff} and N_s. Therefore other situations must be considered.

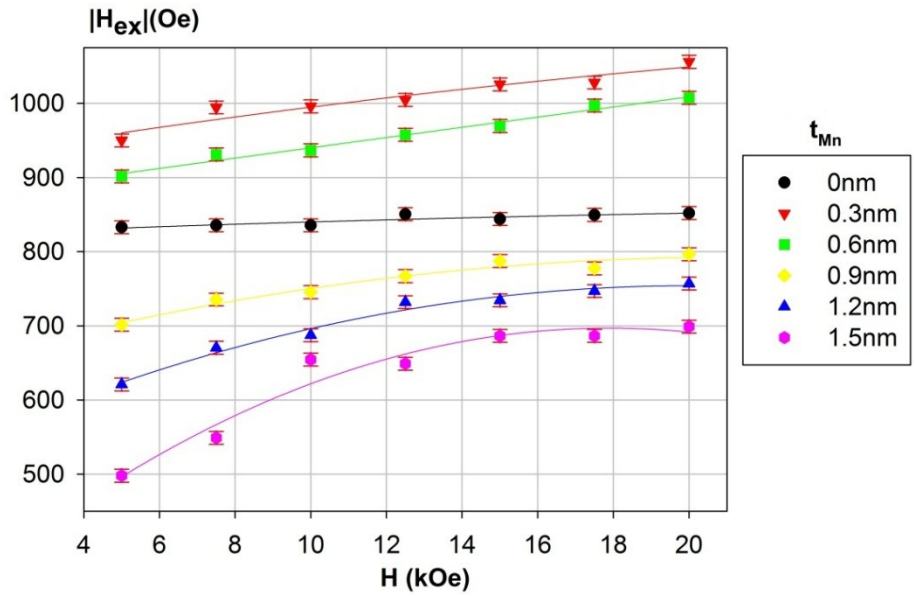

Figure 44: Graph showing the variation in the effect of setting field H_{set} on the loop shift H_{ex} with the addition of 0-5 atomic layers of Mn without removal of the athermal training effect.

A second possibility is that with the addition of Mn there is an increase in disorder within the clusters themselves. As the size of the clusters increases it is unlikely that the spins in the centre of the cluster will experience the same exchange interactions as those at the edge of the cluster. As more Mn is added the spins in

the centre of the cluster will feel a decrease in the exchange interaction from both the F and AF layers. The spins at the edge of the cluster would feel the inverse being more strongly influenced by either the F or AF layers. This would lead to an overall decrease in H_{ex} with increasing Mn thickness. The final possibility is that the clusters themselves interact through dipole-dipole interactions. This would lead to a decrease in the overall order of the clusters providing the shape of the curves as shown in figure 41.

The variation of H_{ex} with respect to H_{set} without the athermal training effect removed is shown in figure 44. The results are very similar; however they consistently seem to contain an additional fluctuation of around ±10 – 15Oe. This additional variability is most likely due to the setting process of the interfacial spins as described in section 3.2.2. Further the increase in H_{ex} in the 1.5nm case is far greater with a change of 201Oe as opposed to the 143Oe as shown in table 5. It is possible that the interfacial spins are far more difficult to set. With the initial application of a high temperature they are able to settle in energetically favourable orientations and upon field cycling there is no longer sufficient energy to return to the previous orientations. This result fits with the spin clusters being misaligned however whether this is due to dipole-dipole interactions between the spin clusters or exchange interactions with the F/AF layers is unclear.

Mn Thickness (nm)	ΔH_{ex} (±14 Oe)	ΔH_{C1} (±14 Oe)
0	19	22
0.3	103	9
0.6	126	-15
0.9	112	-16
1.2	115	21
1.5	143	75

Table 5: Table showing the changes in H_{ex} and H_{c1} with setting field.

The variation in the return branch of hysteresis loop before and after removal of training, ΔH_{C1}, in figure 45 and table 5 lacks overall systematic change, however the large increase in the case of 1.5nm hints that there may be some systematic increase. If the interfacial spins behave as paramagnetic spin clusters then it is

reasonable that low temperatures would be required to properly observe the systematic variation of the training.

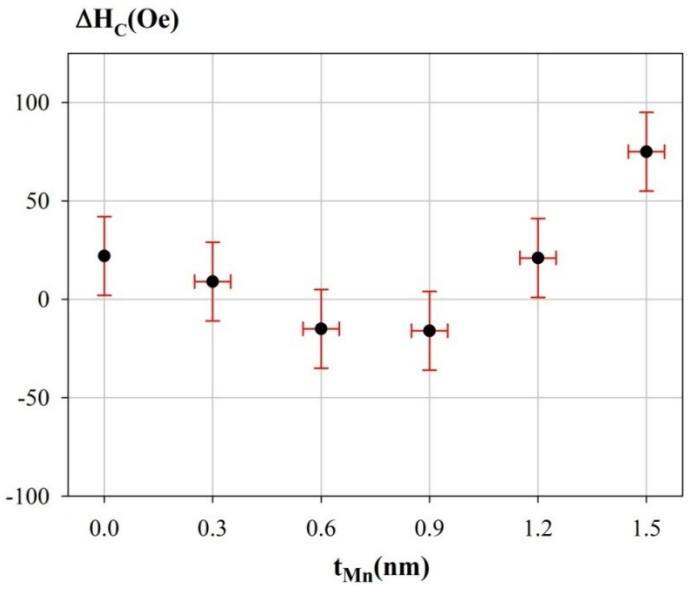

Figure 45: Change in H_{C1} between 5kOe and 20kOe setting fields with respect to Mn interfacial layer thickness.

In this section the effect of inserting 0 to 5 mono layers of Mn at the interface of an IrMn/CoFe bilayer was measured. An increase in H_{ex} of 100 and 50Oe was found with the addition of 1 and 2 monolayers respectively. However subsequent layers decreased H_{ex} by up to 50%. Through analysis of both the grain size and blocking temperature distributions it was found that the modification of the system was solely due to changes in the interface. This was further confirmed by the relationship between H_{set} and H_{ex}. It was found that with the addition of Mn at the interface an increase in H_{ex} of ~125Oe occurred when setting at 20kOe as opposed to 5kOe. A negligible change was observed in the case of 0nm of Mn. It was surmised that the Mn layer caused the size of the interfacial spin clusters to increase as well as changing either the internal spin structure of the clusters or how they interact.

Chapter 6. Conclusion and Future Work

6.1. Effect of Mn

The aim of this study was to attempt to explain the origin of the enhancement of H_{ex} due to the insertion of 1-2 atomic layers of Mn at the interface of an IrMn/CoFe magnetic thin film. This was carried out by carefully sputtering 1-5 atomic layers of Mn in a sample structure of Si(100)/Ta(5nm)/Ru(5nm)/IrMn(10nm) /Mn(*x*nm)/CoFe(2nm)/Ta(5nm). It was found that after setting the samples at 250°C in a 5kOe field an increase in exchange bias, H_{ex}, from (851±10)Oe to (953±10) and (884±10) Oe respectively was found with the addition of 0.3 and 0.6nm of Mn. With subsequent atomic layers H_{ex} is seen to decrease to as low as (559±5)Oe.

The value of the AF anisotropy, K_{AF}, was calculated for the samples by measuring both the grain size and blocking temperature, T_B, distributions. A minimum of 500 grains per sample were imaged using a TEM and the diameters measured using an equivalent circle method. No change in the median grain diameter, D_m, within error was found with the addition of Mn. Through utilisation of the York Protocols a series of thermal activation measurements were carried out. It was found that the median blocking temperature,$\langle T_B \rangle$, did not change, within error, with the addition of Mn. These results were mirrored in the lack of change in K_{AF}. These results suggest that the modification to the system is solely due to changes at the F/AF interface.

As seen in the summary table below the samples are generally highly uniform. This is best seen in the consistency in the values of $\langle T_B \rangle$. However significant changes in the median grain volume, V_m, were noted which may be associated with variations in the temperature in the HiTUS growth system during growth sessions. Typically the RF power used to generate the plasma was 1.5kW which will lead to a significant rise in temperature in the chamber which is $(\sim 60\text{cm})^3$. Although it should also be noted that whilst the range of grain volumes obtained appears significant, it corresponds to a range of diameters differing by less than 2nm.

The effect of the setting field, H_{set}, on the samples was investigated and it was found that when no Mn was added there was, within error, no change in H_{ex} with H_{set}. However with the addition of Mn at the interface a change of up to ~125Oe in H_{ex} occurred when the setting field was measured from 5 to 20kOe. It has been reported in literature by Tsunoda et al. [43] that it is the uncompensated Mn interfacial spins that are responsible for the coupling leading to exchange bias. However Kaeswurm et al. [4] and Fernandez-Outon et al. [36] have found that the interfacial spins act as paramagnetic clusters consisting of 10-50 spins each with a moment of a μ_B. It was initially hypothesised that Mn diffuses through the sample creating a Mn deficiency at the interface. By combining these two ideas it can be seen that the addition of Mn initially corrects for this deficiency and subsequently increases the number of disordered interfacial spins within the clusters. This is seen in the variation of H_{ex} with H_{set} which appears to follow a Langevin type function. This would be expected for paramagnetic spin. This however only explains the shape of the H_{set} curves.

It is also seen from the data in table 6 that the change in H_{ex} with an increase in setting field from 5-20kOe is affected dramatically by the addition of Mn. This supports the concept of quasi-independent interface spin clusters also indicated by the Langevin type behaviour. There also appears to be a correlation between the change in H_{ex} due to setting field, ΔH_{ex}, and V_m although there is insufficient data for this to be confirmed.

Mn Thickness (nm)	H_{ex} (±10 Oe)	K_{AF} (10^6ergs/cc)	$<T_B>$ (±5 K)	V_m (±10% nm^3)	ΔH_{ex} (±14 Oe)
0	851	(9 ± 1)	433	870	19
0.3	953	(8 ± 2)	423	720	103
0.6	884	(7 ± 1)	420	920	126
0.9	720	(8 ± 1)	429	830	112
1.2	709	(8 ± 1)	433	880	115
1.5	559	(6 ± 2)	425	1030	143

Table 6: Summary of results.

6.2. Further Work

The conceptual model of spin clusters has proven its validity through the measurements presented in this work. As such there is a pressing need for a predictive model of the behaviour of interfacial spin clusters. A standard Monte Carlo simulation of the system is called for however as has been demonstrated in this study and in the literature the system is subject to a number of complex interactions. Similarly there is an uncertainty regarding the grain size dependence of the interfacial spin clusters.

Experimentally it is necessary to establish clearly the atomic structure and composition of the interface. Cross sectional TEM imaging of the interface coupled with atomic resolution Energy Dispersive X-Ray (EDX) spectroscopy would provide this information. Information on the spin structure of the interface is also required. This could be achieved through neutron diffraction.

List of Symbols

A

AF	Antiferromagnetic
a_{AF}	Antiferromagnetic Grain Area
AGFM	Alternating Gradient Field Magnetometer
AC	Alternating Current
a	Area

B

B(J,a)	Brillouin Function
BCC	Body Centred Cubic
∇B_0	Field Gradient

C

C	Curie Constant
c	Contact Fraction
C^*	Interfacial Scaling Factor
°C	Degrees Celsius

D

DC	Direct Current
DRAM	Dynamic Random Access Memory
d	Distance Between Crystallographic Planes
D	Grain Diameter
D_m	Median Grain Diameter

E

E_{ex}	Exchange Energy
E	Magneto-Crystalline Anisotropy Energy
E_{EB}	Energy per unit Area of an Exchange Biased System
E_{AF}	Antiferromagnetic Particle Energy
ΔE	Energy Barrier to Reversal
e_A	Range of Anisotropy Energies
Δe	Range of Coupling Energies
e	Induced Voltage

F

F	Ferromagnetic
FET	Field Effect Transistor
f_0	Attempt Frequency
f(V)	Grain Volume Distribution
F_M	Force Due to Magnetisation
f(D)	Grain Diameter Distribution
$f(\Delta E_C)$	Critical Value of Energy Barrier at Setting Temperature

G

GMR	Giant Magneto Resistance
G (e_a,Δe)	Joint Distribution Function

H

HDD	Hard Disk Drive
H_{ex}	Exchange Bias Loop Shift
H	Applied Magnetic Field

H_m	Molecular Field
h	Plank's Constant
H_D	Demagnetising Field
H_C	Coercivity
H^*	Ferromagnetic Layer Exchange Field
H_K^*	Pseudo Anisotropy Field
H_{ex}^i	Intrinsic Exchange Bias
H_{eff}	Effective Exchange Field
HiTUS	High Target Utilisation Sputtering
ΔH_{C1}	Change in the return branch after training is removed

I

IBS	Ion Beam Sputtering

J

J	Angular Momentum Quantum Number
J_K	Uniaxial Anisotropy Constant
J_{ex}	Exchange Integral
J_{INT}	Interfacial Coupling Constant

K

K	Degrees Kelvin
k_F	Fermi Momentum
K_F	Ferromagnetic Anisotropy Constant
K_{AF}	Antiferromagnetic Anisotropy Constant
k_B	Boltzmann Constant
$K_{AF}(T_{meas})$	Antiferromagnet Anisotropy at the Measurement Temperature

Kw	Kilowatt

M

MRAM	Magnetic Random Access Memory
M	Magnetisation
M_S	Saturation Magnetisation
m(t)	Time Dependent Surface Moment of Antiferromagnetic Layer
MOKE	Magneto Optical Kerr Effect
MBE	Molecular Beam Epitaxy
m	Mass
m_{AF}	Antiferromagnetic Sub-Lattice Moment

N

N	Number of Atoms
N_D	Demagnetising Factor
N_{AF}	Number of Antiferromagnetic Particles
N_s	Number of Interfacial Spins

O

Oe	Oersteds

P

P	Paramagnetic
P_S	Saturation Value of the AF Order

R

R	Resistance
ΔR	Change in Resistance
R_A	Interatomic Distance
RF	Radio Frequency
R_{AP}	Anti-Parallel Resistance
R_P	Parallel Resistance
R↑	Spin-up Resistance
R↓	Spin-down Resistance
rpm	Revolutions per Minute
r_a	Atomic Radius
r_{3d}	3d Subshell Radius
RKKY	Theory of Ruderman, Kittel, Kasay and Yoshida

S

S	Spin Quantum Number
S_t	Time Dependent Co-efficient

T

T	Temperature
T_C	Curie Temperature
T_N	Néel Temperature
t_F	Ferromagnetic Layer Thickness
t_{AF}	Antiferromagnetic Layer Thickness
TEM	Transmission Electron Microscope
T_{NA}	Temperature of No Thermal Activation
T_B	Blocking Temperature
$\langle T_B \rangle$	Median Blocking Temperature

t	Time
τ^{-1}	Relaxation Time
T_{set}	Setting Temperature
t_{set}	Setting Time
T_{meas}	Measurement Temperature
t_{set}	Measurement Time
TMR	Tunnelling Magneto Resistance

U

UHV	Ultra High Vacuum

V

V	Voltage
V_F	Volume of Ferromagnetic Layer
V_{AF}	Volume of the Antiferromagnetic Layer
V_{set}	Largest Set Volume
V_C	Minimum Set Volume
VSM	Vibrating Sample Magnetometer
V_S	Sample Volume
v	Velocity
V_m	Median Grain Volume

Z

Z	Atomic Number

αβγ

γ	Molecular Field Co-efficient

σ_s/σ_0	Relative Spontaneous Magnetisation
$\alpha/\beta/\phi/\theta/\psi$	Assorted Angles (usage listed in text)
γ_m	Domain Wall Anisotropy Energy
δ	Minimum Domain Wall Thickness
χ	Susceptibility
ϕ_F	Flux
λ	Wavelength
σ	Standard Deviation of lnD
μ	Mean of lnD
γ_{an}	Anisotropy Energy per Unit Area
μ_B	Bohr Magneton

References

1. *New Magnetic Anisotropy.* **Meiklejohn , W H and Bean, C P.** 5, s.l. : Physical Review, 1956, Vol. 102, pp. 1413-1414.

2. *Exchange Anisotropy - A Review.* **Berkowitz, A E and Takano, Kentaro.** s.l. : Journal of Magnetism and Magnetic Materials, 1999, Vol. 200, pp. 552-570.

3. *A New Paradigm for Exchange Bias in Polycrystalline Thin Films.* **O'Grady, K, Fernandez-Outon, L E and Vallejo-Fernandez, G.** 2009, Journal of Magnetism and Magnetic Materials. doi:1-.1016/j.jmmm.2009.011.

4. *The Origin of Training in Polycrystalline Metallic Exchange Biased Thin Films.* **Kaeswurm, B and O'Grady, K.** Physical Review Letters - Currently under review.

5. *The Discovery, Development and Future of GMR: The Nobel Prize 2007.* **Thompson, S.** 093001, 2008, Journal of Physics D: Applied Physics, Vol. 41.

6. *Electrical Conductivity in Transition Metals.* **Mott, M F.** 1936, Proceedings of the Royal Society London A, Vol. 153, p. 669.

7. *Recording Physics of Perpendicular Media: Soft Underlayers.* **Litvinov, D, Kryder, M H and Khizroev, S.** 2001, Journal of Magnetism and Magnetic Materials, Vol. 232, pp. 84-90.

8. **Hitachi.** [Online] [Cited: August 18, 2011.] https://www1.hitachigst.com/hdd/technolo/overview/chart13.html.

9. *Neutron Diffraction Study of y-Phase Mn-Ir Single Crystals.* **Yamaoka, T, Mekata, M and Takaki, H.** 1973, Journal of the Physical Society of Japan, Vol. 36, pp. 438-444.

10. *Development of the Magnetic Tunnel Junction MRAM at IBM: From First Junctions to a 16-Mb MRAM Demonstrator Chip.* **Gallagher, W J and Parkin, S S. P.** 1, January 2006, IBM Journal of Research and Development, Vol. 50.

11. *Non-Volatile Magnetic Random Access Memories (MRAM).* **Sousa, R C and Prejbeanu, I L.** s.l. : C. R. Physique, 2005, Vol. 6.

12. *Current-Driven Magnetisation Reversal and Spin-Wave Excitations in Co/Cu/Co Pillars.* **Katine, J A, et al.** 14, 2000, Physical Review Letters, Vol. 84, pp. 3149-3152.

13. **Cullity, B D.** *Introduction to Magnetic Materials.* s.l. : Addison-Wesley, 1972. 0-201-01218-9.

14. **Heisenburg, W.** 1928, Z. Physics, Vol. 49, p. 619.

15. *Indirect Exchange Coupling of Nuclear Magnetic Momens by Conduction Electrons.* **Ruderman, M A and Kittel, C.** 1, 1954, Physical Review, Vol. 96, pp. 99-102.

16. **Yosida, K.** 1957, Physical Review, Vol. 96, p. 99.

17. *Magnetic Properties of Cu-Mn Alloys.* **Yosida, K.** 5, 1957, Physical Review, Vol. 106, pp. 893-898.

18. **O'Handley, R C.** *Modern Magnetic Materials: Principles and Applications.* s.l. : John Wiley & Sons, 2000. 0-471-15566-7.

19. *Influence des Fluctuations du Champ Moleculaire sur les Proprietes Magnetiques des Corps.* **Neel, L.** 1932, Annales de Physique, Vol. 18, pp. 5-105.

20. *Etude Theorique du Couplage Ferro-AntiFerromagnetique dans les Couches Minces.* **Neel, L.** Paris : s.n., 1967, Annals of Physics , Vol. 2, pp. 61-80.

21. *Thermal Fluctuation Afteraffect Model for Some Systems with Ferromagnetic-Antiferromagnetic Coupling.* **Fulcomer, E and Charap, S H.** 10, s.l. : Journal of Applied Physics`, 1972, Vol. 43.

22. *Temperature and Frequency Dependence of Exchange Anisotropy Effects in Oxidized NiFe Films.* **Fulcomer, E and Charap, S H.** 10, s.l. : Journal of Applied Physics, 1972, Vol. 43, pp. 4184-4190.

23. *Simple Model for THin Ferromagnetic Films Exchange Coupled to an Antiferromagnetic Substrate.* **Mauri, D, et al.** 7, 1987, Journal of Applied Physics, Vol. 62, pp. 3047-3049.

24. *Random-Field Model of Exchange Anisotropy at Rough Ferromagnetic-Antiferromagnetic Interfaces.* **Malozemoff, A P.** 7, 1987, Physical Review B, Vol. 35, pp. 3679-3682.

25. *Coupling Mechanisms in Exchange Biased Films.* **Schulthess, T C and Butler, W H.** 8, 1999, Journal of Applied Physics, Vol. 85, pp. 5510-5515.

26. *Domain State Model for Exchange Bias.* **Nowak, U, et al.** 2002, Physical Review B, Vol. 66.

27. *Diluted Antiferromagnets in Exchange Bias: Proof of the Domain State Model.* **Miltenyi, P, et al.** 18, 2000, Physical Review Letters, Vol. 84, pp. 4224-4227.

28. *Exchange Anisotropy - A Review.* **Meiklejohn, W H.** 3, March 1962, Journal of Applied Physics, Vol. 33, pp. 1328-1335.

29. **Yelon, A, Francombe, M H and Hoffman, R W.** *Physics of Thin Films.* s.l. : Academic, 1971. Vol. 6.

30. *Orientational Dependence of the Exchange Biasing in Molecular Beam Epitaxy Grown Ni(80)Fe(20)/Fe(50)Mn(50) Bilayers.* **Jungblut, R, et al.** 75, May 1994, Journal of Applied Physics, pp. 6659-6664.

31. *Exchange Anisotropy in Mixed Manganites with the Hasmannite Structure.* **Jacobs, I S and Kouvel, J S.** 2, April 1961, Physical Review, Vol. 122, pp. 412-418.

32. *Thermally Assisted Reversal of Exchange Biasing in NiO and FeMn Based Systems.* **van der Heijden, P A. A., et al.** 1997, Applied Physics Letters, Vol. 72, pp. 492-494.

33. *Defect and Impurity Effects in Exchange Bias Systems.* **Vallejo-Fernandez, G, Kaeswurm, B and O'Grady, K.** 2011, Journal of Applied Physics, Vol. 109.

34. *L12 Phase Formation and Giant Exchange ANisotropy in Mn3Ir/CoFe Bilayers.* **Tsunoda , M, et al.** 2006, Journal of Magnetism and Magnetic Materials, Vol. 304, pp. 55-59.

35. *Effect of the Ferromagnetic Layer Thickness of the Blocking Temperature in IrMn/CoFe Exchange Couples.* **Vallejo-Fernandez, G, et al.** 11, 2008, IEEE Transactions on Magnetics, Vol. 44, pp. 2835-2838.

36. *Interfacial Spin Order in Exchange Biased Systems.* **Fernandez-Outon, L E, et al.** 093907, 2008, Journal of Applied Physics, Vol. 104.

37. *Symmetry Driven Irreversibilities at Ferromagnetic-Antiferromagnetic Interfaces.* **Hoffmann, A.** 9, 2004, Physical Review Letters, Vol. 93.

38. *Interfacial Uncompensated Antiferromagnetic Spins: Role in Unidirectional Anisotropy in Polycrystalline NiFe/CoO Bilayers.* **Takano, K, et al.** 6, 1997, Physical Review Letters, Vol. 79.

39. *Texture Effects in IrMn/CoFe Exchange Bias Systems.* **Aley, N P, et al.** 11, s.l. : IEEE Trans. Mag., 2008, Vol. 44.

40. *Compositional Dependence of Antiferromagnetic Anisotropy in IrMn/CoFe Exchange Bias Systems.* **Aley, N P and O'Grady, K.** 07D719, 2011, Journal of Applied Physics D, Vol. 109.

41. *First-Principles Study of the Magnetic Structures of Ordered and Disordered Mn-Ir Alloys.* **Sakuma, A, et al.** 024420, 2003, Physical Review B, Vol. 67.

42. *Uncompensated Anitferromagnetic Spins at the Interface in Mn-Ir Based Exchange Biased Layers.* **Tsunoda, M, et al.** 2007, Journal of Applied Physics, Vol. 101.

43. *Linear Correlation Between Uncompensated Antiferromagnetic Spins and Exchange Bias in Mn-Ir/Co(100-x)Fe(x) Bilayers.* **Tsunoda, M, et al.** 2010, Applied Physics Letters, Vol. 97.

44. *Enhancement of Exchange Bias by Ultra-Thin Mn Layer Insertion at the Interface of Mn-Ir/Co-Fe Bilayers.* **Tsunoda, M, et al.** 12, 2007, Physica Status Solidi b, Vol. 244.

45. *Exchange Bias Interactions in Polycrystalline/Amorphous Bilayers.* **Dean, J., et al.** 072504, 2010, App. Phys. Lett, Vol. 96.

46. *The Formation Mechanism of 360 Domain Walls in Exchange-Biased Polycrystalline Ferromagnetic Films.* **Dean, J, et al.** 073901, 2011, J. Appl. Phys., Vol. 110.

47. *Exchange-bias in Amorphous Ferromagnetic and Polycrystalline Antiferromagnetic Bilayers: Structural Study and Micromagnetic Model.* **Kohn, A, et al.** 083924, 2011, J. Apply. Phys, Vol. 109.

48. **Chow, P P.** Molecular Beam Epitaxy. [book auth.] John L Vossen and Werner Kern. *Thin Film Processes II.* s.l. : Academic Press, Inc., 1991.

49. **Stuart, R V.** *Vacuum Technology, Thin Films and Sputtering: An Introduction.* Minneapolis : Academic Press, 1983. 0-12-674780-6.

50. **Thwaites, M J.** *High Density Plasmas. 6463873* USA, October 15, 2002. Patent.

51. *Deposition of Polycrystalline Thing Films with Controlled Grain Size.* **Vopsaroiu, M, et al.** s.l. : Journal of Physics D: Applied Physics, 2004, Vol. 38, pp. 490-496.

52. *Effect of Cu Impurities on Kaf in IrMnCu/CoFe Exchange Bias Systems.* **Aley, N P, et al.** 10, York : IEEE Trans. Mag., 2009, Vol. 45.

53. **Crangle, John.** *Solid State Magnetism.* London : Edward Arnold, 1991. 0-340-54552-6.

54. **Goodhew, Peter J, Humphreys, John and Beanland, Richard.** *Electron Microscopy and Analysis.* London : Taylor and Francis, 2001. 0-203-18425-4.

55. **Williams , David B and Carter, Barry C.** *Transmission Electron Microscopy 3: Imaging.* New York : Plenum Press , 1996. 0-306-45324-X.

56. *Determination of Grain Size Distributions in Thin Films.* **Jones, G R, Jackson, M and O'Grady, K.** 1999, Journal of Magnetism and Magnetic Materials, Vol. 193, pp. 75-78.

57. *Control of the Setting Process in CoFe/IrMn Exchange Bias Systems.* **Vallejo-Fernandez, G, et al.** 033906, 2008, Journal of Applied Physics, Vol. 104.

58. *Effect of the Ferromagnetic Layer Thickness on the Blocking Temperature in IrMn/CoFe Exchange Couples.* **Vallejo-Fernandez, G, et al.** 11, 2008, IEE Transactions on Magnetics, Vol. 44, p. 2835.

59. *Temperature Dependence of Exchange Bias in Polycrystalline Ferromagnet-AntiFerromagnet Bilayers.* **Stiles, M D and McMichael, R D.** 18, 1999, Physical Review B, Vol. 60, p. 12950.

60. *Controlled Enhancements or Suppression of Exchange Biasing using Inpurity delta Layers.* **Ali, M, Marrows, C H and Hickey, B J.** s.l. : Physical Review B, 2008, Vol. 77. 134401.

61. *Interface and Microstructure Evolutions in Synthetic Ferrimagnet-Based Spin Valves Upon Exposure to Postdeposition Annealing.* **Kim, Y. K., et al.** 10, 2003, J. App. Phys., Vol. 93.

62. *CoFe/IrMn Exchange Biased Top, Bottom and Dual Spin Valves.* **Anderson, G, Huai, Y and Miloslawsky, L.** 9, 2000, Journal of Applied Physics, Vol. 87, pp. 6989-6991.

63. *Seedlayer and Preheating Effects on Crystallography and Recording Performance of CoCrPtB Perpendicular Media.* **Zheng, M, et al.** 5, 2002, IEEE Transactions on Magnetics, Vol. 38.

64. *Private Communications.* **Cramp, N.**